SANDIA REPORT
SAND2021-14167
Printed November 2021

Sandia National Laboratories

High-Brightness Ultraviolet Lasers for Leap-Ahead National Security Applications

Erik J. Skogen, Seth A. Fortuna, Andrew A. Allerman, Michael L. Smith, Charles Alford, Mary H. Crawford

Prepared by
Sandia National Laboratories
Albuquerque, New Mexico
87185 and Livermore,
California 94550

Issued by Sandia National Laboratories, operated for the United States Department of Energy by National Technology & Engineering Solutions of Sandia, LLC.

Available to DOE and DOE contractors from
U.S. Department of Energy
Office of Scientific and Technical Information
P.O. Box 62
Oak Ridge, TN 37831

Telephone: (865) 576-8401
Facsimile: (865) 576-5728
E-Mail: reports@osti.gov
Online ordering: http://www.osti.gov/scitech

Available to the public from
U.S. Department of Commerce
National Technical Information Service
5301 Shawnee Rd
Alexandria, VA 22312

Telephone: (800) 553-6847
Facsimile: (703) 605-6900
E-Mail: orders@ntis.gov
Online order: https://classic.ntis.gov/help/order-methods/

ABSTRACT

In this project we endeavored to improve the state-of-the-art in UV lasers diodes. We made important advancements in several fronts from modeling, to epitaxial growth, to fabrication, and testing. Throughout the project it became clear that polarization doping would be able to help advance the state of laser diode design in terms of electrical performance, but the optical design would need to be investigated to ensure that a 2D guided mode would be supported. New capability in optical modeling using commercial software demonstrated that the new polarization doped structures would be viable. New capability in pulsed testing was established to reach the current and voltage required. Our fabricated devices had some parasitic electrical paths which hindered performance that we were ultimately unable to overcome in the project timeframe. We do believe that future projects will be able to leverage the advancements made under this project.

CONTENTS

LIST OF FIGURES

LIST OF TABLES

This page left blank

ACRONYMS AND DEFINITIONS

Abbreviation	Definition
BCB	benzocyclobutene
BOE	buffered oxide etch
CL	cathodoluminescence
DUT	device under test
FDTD	finite difference time domain
ICP	inductively coupled plasma
LIV	light-current-voltage
LOC	large-optical-cavity
MQW	multiple-quantum-well
NIC	Nomarski interference contrast
PCB	printed circuit board
PECVD	plasma-enhanced chemical vapor deposition
PL	photoluminescence
PR	photoresist
RIE	reactive ion etch
RWG	ridge waveguide
SEM	scanning electron microscope
SIMS	secondary ion mass spectroscopy
TE	thermo-electric
TLM	transfer length method
UV	ultra-violet

1. INTRODUCTION

Since the first demonstration of III-Nitride semiconductor lasers 20 years ago, there have been great strides in improving the efficiency and output power of blue laser diodes based on InGaN/GaN. Moving into the ultra-violet (UV) region of the spectrum requires higher bandgap AlGaN alloys which have significantly greater materials challenges than their blue-emitting InGaN counterparts. As a result, performance metrics of electrically-pumped UV lasers drop rapidly, at the start of the LDRD reaching the limit of ~336 nm as the shortest wavelength reported for quantum well UV laser diodes [1] and later reaching 271.8 nm [2].

Throughout this program we targeted two fundamental thrust areas, (1) novel UV laser physics/design/architecture called *Novel UV laser Architecture* and (2) advanced III-nitride materials epitaxy called *Strategic III-Nitride Materials Growth*. As it stands, Sandia is at the forefront of AlGaN materials epitaxy, one of the world leaders. Sandia also holds a good deal of experience and expertise in advanced III-(As/P) laser design. We used these areas of expertise to design and epitaxially grow laser structures that take advantage of these concepts.

Our scope ranged from initial concepts, including the large optical cavity (LOC) and vertical current injection using conducting GaN substrates, to modeling/simulation, epitaxial growth techniques, fabrication, and testing. Along the way we incorporated a polarization doping technique that had been gaining popularity in literature and adapted our laser architecture to include this concept. Advancements in the modeling of the optical and electrical aspects of the laser design were explored using commercial software that was extended to capture some of the unique aspects of hexagonal III-N materials. We were able to make great strides in the epitaxial growth of these materials on electrically conducting GaN substrates and explored new methods to reduce epilayer cracking and improve surface morphology. The creation of a new test capability was established to achieve both the high-current and high-voltage sub-microsecond pulsing to test these structures. Although we did not have a diode device reach laser threshold conditions, we did demonstrate key device characteristics that preceded laser emission. We believe that with further refinement of the laser cavity and/or improvement of the modal gain, and with the reduction of parasitic diodes through advanced processing techniques we could eventually reach the goal we set out to achieve. Nevertheless, the advancements we made throughout this project will have positive impact for future projects.

2. EXPERIMENTAL

Our approach for the project spanned the full development cycle from design -to- modeling/simulation -to- epitaxial growth -to- fabrication and testing. The concepts for a large-optical-cavity (LOC) and the epitaxial growth on GaN substrates for vertical current flow were already established in the proposal, but both the electrical and optical designs required further study to incorporate the remainder of the laser structure design. During the project we also explored polarization doping, a method to achieve mobile holes using AlGaN compositional gradients. The polarization doping concept was explored within a laser structure architecture and simulated both optically and electrically. Epitaxial growth explored both methods to reduce epitaxy cracking and the polarization doping in III-N structures. Finally, the modeling and growth were combined to explore laser structures experimentally.

2.1. Modeling and Simulation

Our approach to modeling laser structures took two primary approaches: first, electrical and bandgap modeling, second, optical modeling. The electrical and bandgap modeling primarily used the commercial software package SiLENSe. The optical modeling primarily used the commercial software package Lumerical. Each of these modeling areas are summarized in the following sections.

2.1.1. Electrical Modeling

The electrical modeling primarily used the commercial software package SiLENSe which aided in the modeling and simulation in several different areas including; polarization doping, carrier concentrations in forward bias, current density calculations in forward bias, injection efficiency calculations, wave-function overlap, and emission wavelength.

The concept of polarization doping has been in literature for some time now and was summarized nicely by Simon, *et. al.* [3]. This polarization doping concept can be summarized by noting that in a compositional grade in a polar material, the polarization charge dipoles are unbalanced and therefore accumulate resulting in a net polarization induced charge regions. These charge regions result in an electric field and ultimately leading to field-induced hole ionization from the deep acceptor states and/or other deep states. This has profound implications in device design by reducing the needed impurity concentration for achieving a given level of mobile hole carrier concentration. We used SiLENSe to model and simulate the structure and experimental results from [3] at room temperature. As shown in the figure, the simulated structure with compositional grade results in a hole carrier concentration of 2e18 cm^3 and is in agreement with the experimental results in [3]. The polarization doping concept was further experimentally explored during this program and described in detail in section 2.1.2, *AlGaN Material Growth – Polarization p-type Doping for Optical Cladding.*

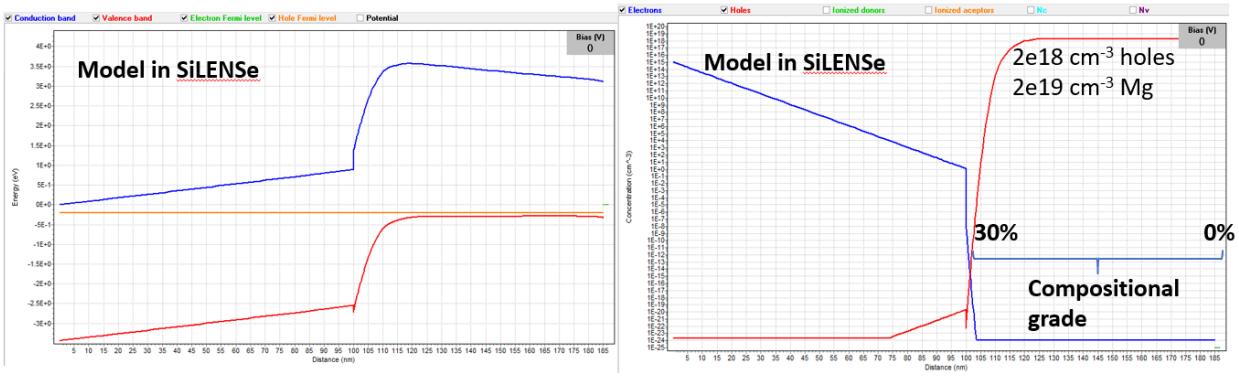

Figure 2-1. Band diagram modeled in SiLENSe of the structure shown in [3] (left). Carrier concentration of the structure showing 2e18 cm^3 holes and is in agreement with the experimental results presented in [3].

Once the polarization doping was demonstrated to be functional, we desired to incorporate this concept into a laser design. There were several laser design challenges that needed to be overcome to include polarization doping. These design challenges included both optical and electrical components; the optical considerations are described in the following section, here, we describe the electrical/carrier implications. While the polarization doping concept can greatly improve the hole concentration with respect to a given Mg concentration in the p-cladding, the transition from a large bandgap near the multiple-quantum-well (MQW) active region was cause for concern due to the potential for carrier pile-up at the heterointerface. Figure 2-2 shows the area of concern as a shaded red region at the transition from the p-cladding to the MQW.

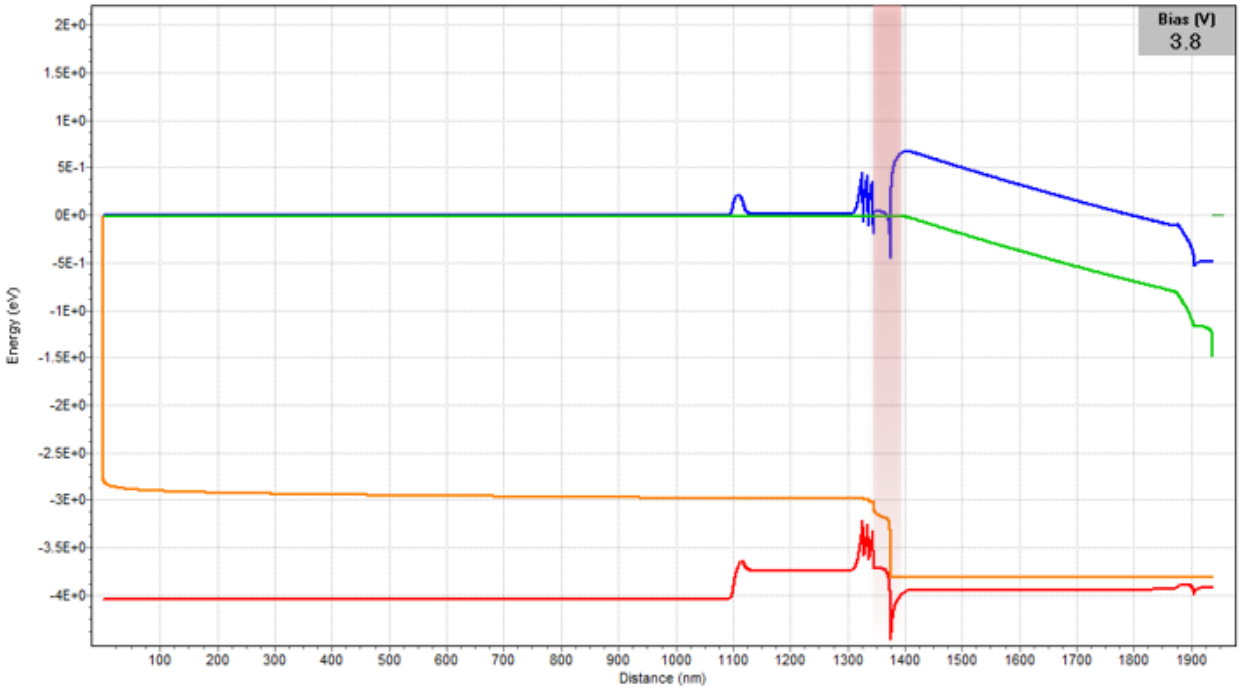

Figure 2-2. Band diagram of a LOC laser design with polarization doping grade in the p-cladding. Shaded region indicates a non-ideal transition from p-cladding to MQW.

We explored how to improve transition from the MQW region -to- the p-cladding region using several metrics including, current density at a given applied bias, non-uniformity across the MQW set, and computed injection efficiency into the MQW active region. After many iterations we found that adding p-type doping to the 200 Å region between the MQW and the p-cladding offered the best solution resulting in an increase of the current density by a factor of 100,000 at a bias of 3.8 V. This improved injection was also manifested in an improved hole concentration in the quantum wells. We also observed an improvement of the uniformity of the wavefunction and emission wavelength of the quantum wells at that same applied bias. Finally, we also improved the effectiveness of the electron block function as indicated by a lower electron population beyond the MQW region. The new design is shown in Figure 2-3.

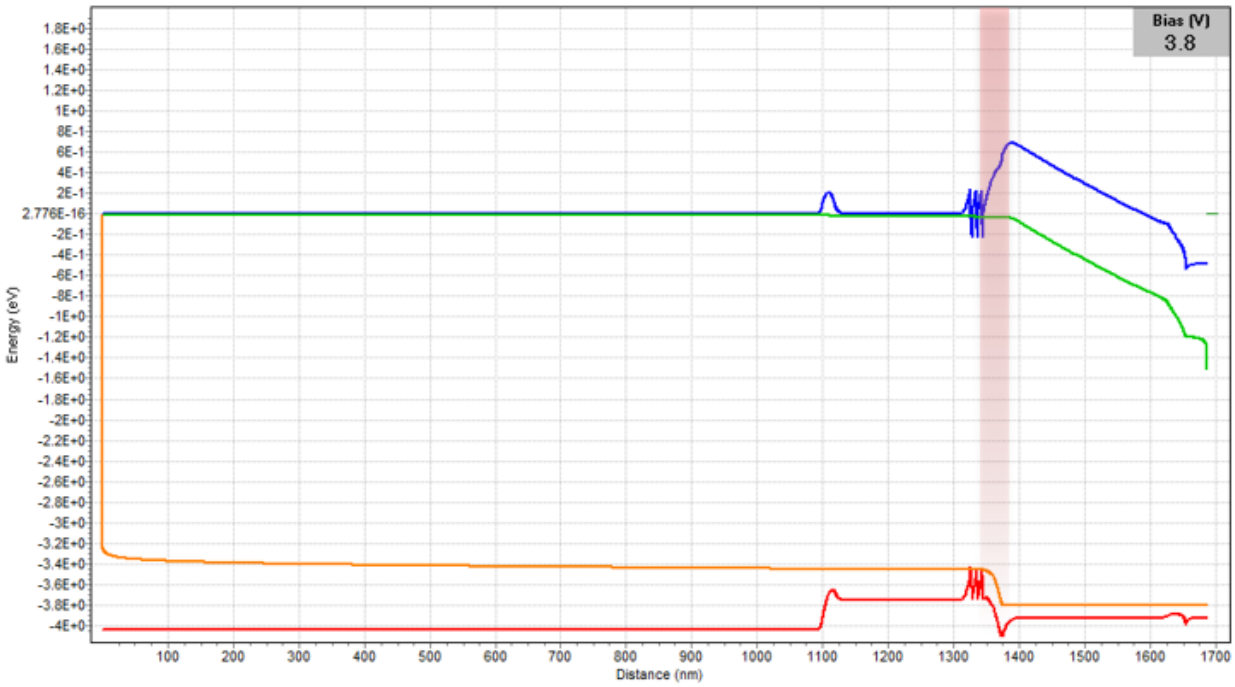

Figure 2-3. Band diagram of the improved laser design (over that shown in Figure 2-2) showing the difference in the transition region (shaded red) between the MQW and the p-cladding.

The new design was explored by changing the location of the doping in the 200 Å layer that follows the MQW and was verified experimentally. Three AlGaN laser samples demonstrate the effectiveness of the proximity of the doping to the MQW; as the proximity of the doping moves closer to the MQW region, the intensity of the measured electroluminescence improves, see Figure 2-4. It is also observed that the ratio of emission near 350 nm to emission near 500 nm is improved with doping proximity which indicates that the carriers are more efficiently recombining in the desired active region instead of at mid-gap states.

We also investigated the evolution of the relative emission efficiency of the active region to that of mid-gap states by taking spectra for a series of injection currents as shown in Figure 2-5. In the figure we are comparing the electroluminescence for two samples with different doping setbacks. In sample VNA7821 the doping setback from the MQW region is 25 Å, while the doping setback for VNA7828 is ~12 Å. As shown in the figure, the sample with doping setback of 25 Å has greater emission efficiency than the 12 Å setback sample both relative to the mid-gap emission wavelength range (~500

nm) and in photons/electron. This shows that the precise doping location is critical to achieving optimal electroluminescence performance.

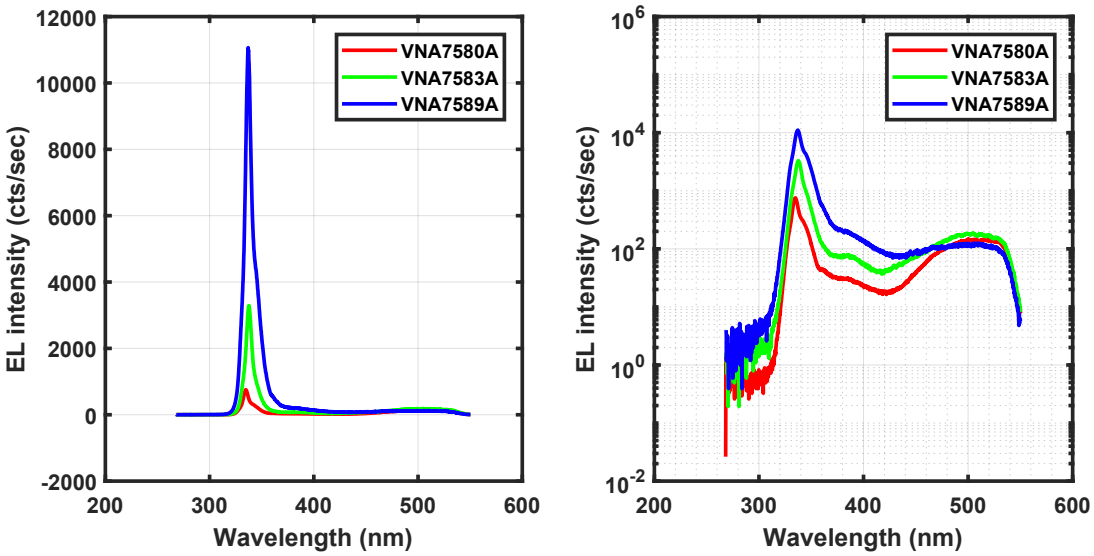

Figure 2-4. Electroluminescence of three samples were the p-type doping adjusted in the 200 Å region between the p-cladding and the MQW. Sample VNA7580A was not intentionally doped in the transition layer. The next two samples moved the p-type doping progressively closer to the MQW.

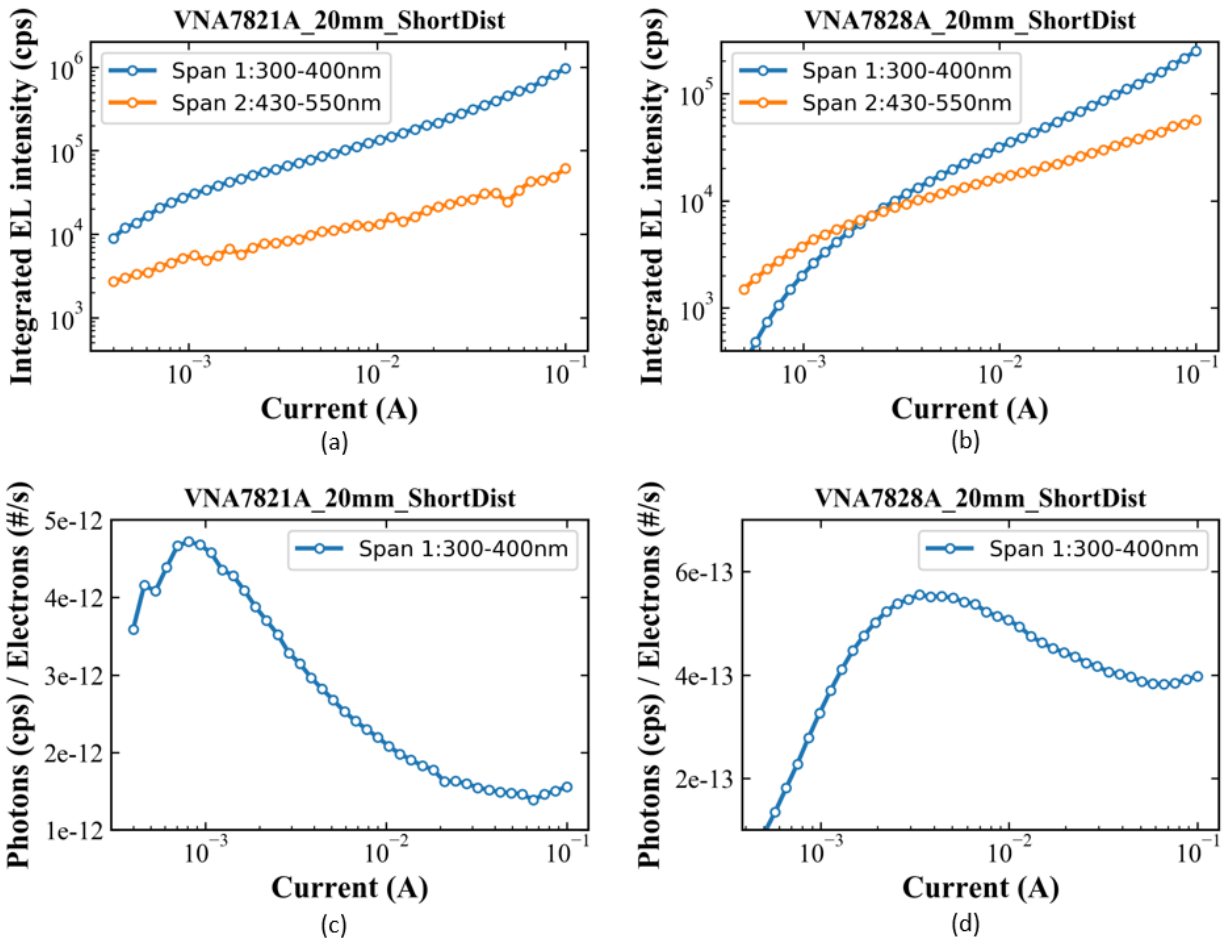

Figure 2-5. Electroluminescence as a function of current for samples with different Mg doping proximity from the MQW region; 25 Å for VNA7821 and 12 Å for VNA7828. a) Electroluminescence for the wavelength region of interest (blue) and wavelength region of parasitic recombination due to mid-gap states (orange) showing that the wavelength region of interest maintains much higher emission intensity that the mid-gap states. B) Similar to (a), showing that the emission at the wavelength of interest is much lower efficiency overall and lower that the mid-gap states at low currents. C) relative efficiency of the wavelength region of interest showing nearly an order of magnitude greater efficiency than that shown in (d).

2.1.2. Optical Modeling

The optical modeling of the UV laser structures was primarily targeting the transverse mode simulation. The transverse mode is of particular interest in our approach to laser design as we aim to limit the mode overlap with the p-type cladding and avoid or limit the optical losses that typically accompany high doping concentrations. We used the LOC design strategy to reduce the optical mode overlap with the p-type cladding over more traditional designs. This method necessarily trades optical confinement factor (mode overlap with the gain region) for reduction of optical mode overlap with the p-type cladding. This concept is demonstrated in Figure 2-6 where the thickness of the waveguide core is varied, and the optical mode overlap with the gain and p-type cladding is plotted. Table 2-1 shows the calculated optical mode overlap of both the fundamental mode with the gain region and

the fundamental and second order mode overlap with the p-type cladding. As is evident from the figure and the table, we can greatly reduce the optical mode overlap with the p-cladding by increasing the waveguide core thickness.

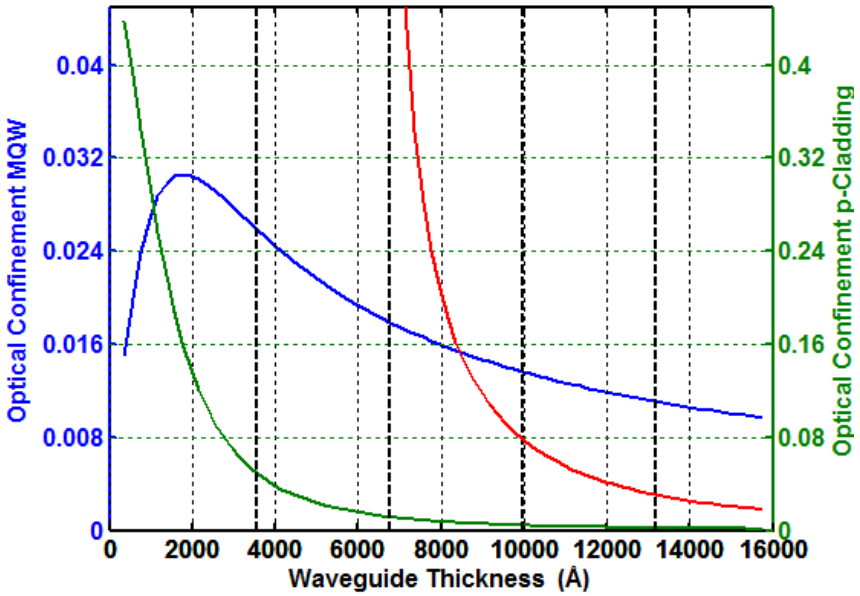

Figure 2-6. Optical confinement factor in both the gain region (MQW) and the p-cladding region as a function of waveguide core thickness.

Table 2-1. Optical mode overlap of selected waveguide core thicknesses.

Waveguide Thickness (Å)	Γ MQW 0th order	Γ p-clad 0th order	Γ p-clad 2nd order
1765	3.0%	18.6%	N/A
2665	2.8%	10.3%	N/A
3805	2.5%	5.1%	N/A
7705	1.6%	1.03%	50%

In Figure 2-7. Traditional design (left) showing a waveguide core thickness that maximizes the optical mode overlap with the gain region, and LOC design (right) showing a waveguide core thickness that trades optical mode overlap of the gain region to reduce the optical mode overlap in the p-cladding region., the 1D refractive index and optical mode is plotted as a function of vertical distance through the structure showing the difference between a traditional design, where one seeks to maximize the optical mode overlap with the gain region, and the LOC design, where one trades optical mode overlap with the gain region for reduced mode overlap with the p-cladding. The waveguide core thickness in the traditional design has an optical mode overlap with the gain region of 3.0% and an optical mode overlap with the p-cladding of >18%. The LOC design reduces the optical mode overlap with the gain region by ~2x but in return reduces the optical mode overlap with the p-cladding by 17 percentage points.

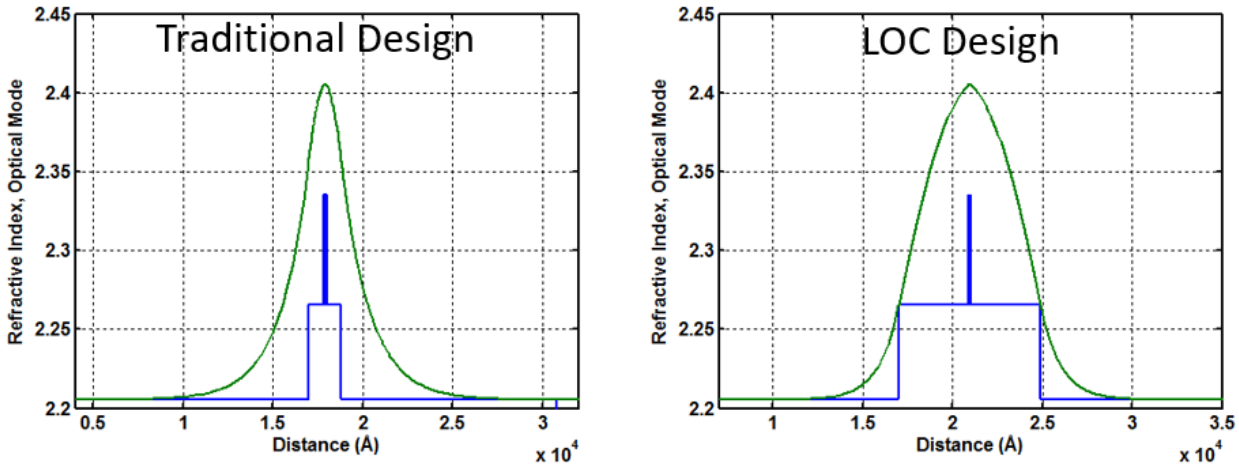

Figure 2-7. Traditional design (left) showing a waveguide core thickness that maximizes the optical mode overlap with the gain region, and LOC design (right) showing a waveguide core thickness that trades optical mode overlap of the gain region to reduce the optical mode overlap in the p-cladding region.

Moving from the 1D models to the 2D models required the additional complication of directional birefringence. In this case, since we are growing on the c-plane of the hexagonal form of III-N, we have a different refractive index in the c-direction from that of the a- and m-directions. The capability to model birefringent materials exists in Lumerical, but we needed to add the refractive index as a function of both Al-content and direction. We were then able to use the 2D waveguide models to simulate the optical mode. A 1D cross-section through the center of a ridge waveguide structure is shown in Figure 2-8. As shown in the figure, there is are two refractive index lines, one pertaining to the extraordinary refractive index and the other pertaining to the ordinary refractive index. It is very important to include this birefringence in any 2D optical mode simulation.

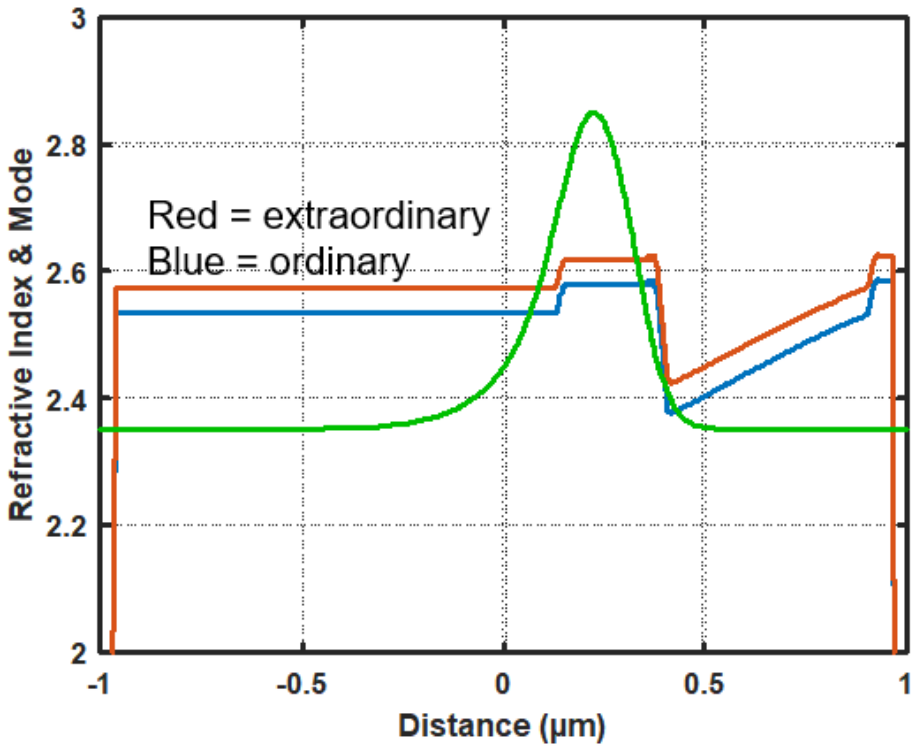

Figure 2-8. 1D cross-section of the refractive index and optical mode (green) as a function of distance in the epitaxial growth direction. Refractive index is plotted for both the extraordinary (red) and ordinary (blue) optical axis.

As shown in the electrical modeling section, the polarization doping can be advantageous for generating mobile holes in the p-cladding region. Because we are growing on the Ga-face, the polarization doping to generate holes requires that the Al concentration grade be high near the waveguide and lower near the p-contact. This results in a low refractive index near the waveguide core and a higher refractive index near the p-contact which is the inverse of what is traditionally used as a graded index-type waveguide. We used 2D optical models to simulate the effect of this inverse refractive index grade and to assess the impact. Figure 2-9 shows the 2D refractive index cross-section and the associated fundamental optical mode of a representative structure. As shown in the figure, the fundamental optical mode is supported in this structure and the penetration of the optical mode into the p-cladding is suppressed even further due the refractive index compositional grade. The majority of the designs that were explored in this program were based on these fundamental designs.

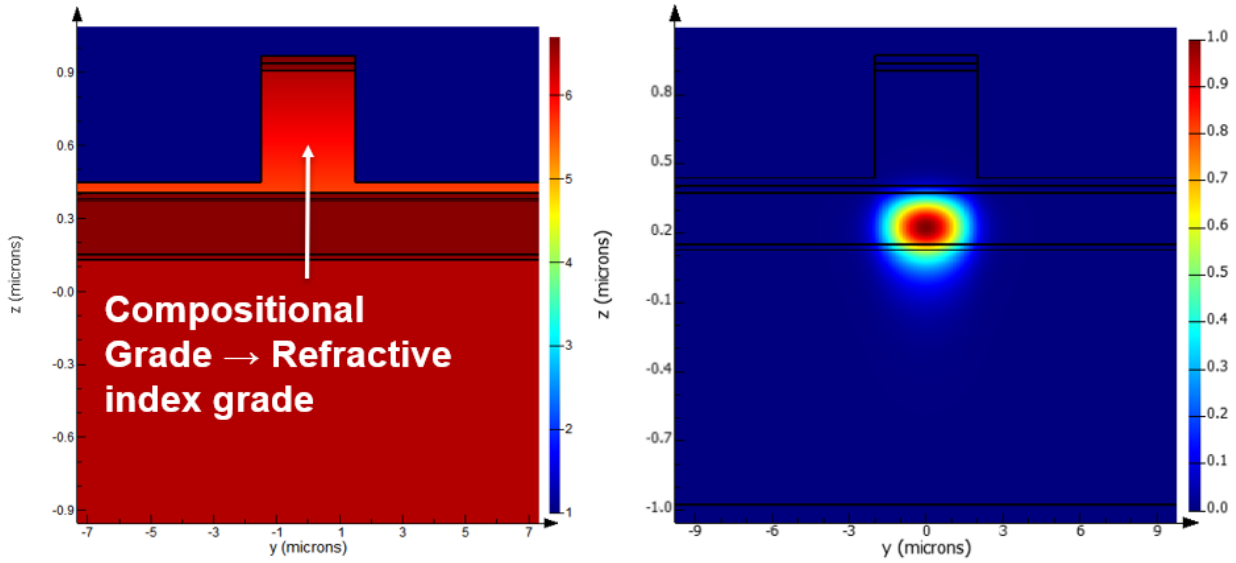

Figure 2-9. Refractive index cross-section of ridge waveguide design featuring the compositional grade in the p-type cladding (left). Simulated fundamental optical mode of the same waveguide cross-section (right).

2.1. AlGaN Material Growth

The $Al_xGa_{1-x}N$ alloy system continues to be the most promising candidate for solid-state, injection laser diodes with emission from 340 nm to 360 nm. However, there are significant material challenges that must be mitigated to realize efficient laser diode sources. These include growth of vertically conducting emitter structures and effective p-type doping. Typical light emitting diodes with emission spanning UVA though UVC bands rely on $Al_xGa_{1-x}N$ based heterostructures grown on sapphire substrates. However, the electrically insulating nature of sapphire substrates requires the use of top-side contacts which suffer from high resistance along the lateral current path leading to poor current spreading and excess heating. Heteroepitaxy of an AlGaN emitter on conducting GaN substrates circumvents the lateral spreading current resistance problem by allowing for vertical conduction in a much more conductive pathway. Other groups have shown that vertical current paths have dramatic effects on the performance of laser diodes [4, 1, 5, 6, 7]. The vertically injected lasers operated up to 10x higher current resulting in 3x higher output power demonstrating the advantages of vertically injected AlGaN lasers. We discuss the development of the growth of $Al_{0.3}Ga_{0.7}N$ epilayers on conducting GaN substrates that allowed us to grow vertically conducting laser diode heterostructures in 2.1.3, Figure 2-10.

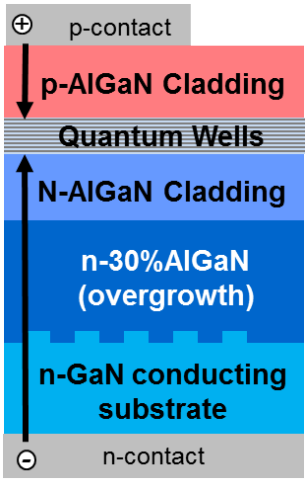

Figure 2-10. Schematic of a vertically conducting UV laser heterostructure enabled by AlGaN growth on patterned, free standing n-type GaN substrates.

In typical AlGaN laser designs, hole injection and optical confinement is achieved with a p-type doped cladding on top of the quantum wells. Unfortunately, acceptor impurities have a very large activation energy in $Al_xGa_{1-x}N$ alloys resulting in optical claddings with poor p-type conductivity which result in high operating voltages and ohmic heating. We circumvented this problem by utilizing compositionally graded, wurtzite AlGaN alloys grown on (0001) plane. The resulting fixed polarization field effectively field ionizes the Mg acceptors resulting in much higher p-type conductivity. Polarization p-type doping is described in 2.1.2.

The composition of $Al_xGa_{1-x}N$ epilayers was measured with a Philips X'Pert Pro diffractometer equipped with a hybrid monochromator and an asymmetric (220) Ge diffracted-beam analyzer using $\omega/2\theta$ scans about the (00.4) and (10.1) reflections of the AlGaN. Al composition was confirmed by room temperature photoluminescence (PL) measurements using a Nanometrics RPM2000 PL mapper employing a 266-nm pump laser. The surface morphology was evaluated using Nomarski interference contrast (NIC) microscopy and atomic force microscopy (AFM). Secondary Ion Mass Spectroscopy (SIMS) was used to measure the concentration of Mg and Si dopants.

GaN-AlGaN multi-quantum well (MQW) structures designed for 340-360 nm emission were characterized by room temperature photoluminescence to determine emission wavelength, peak intensity, and full-width-half-max linewidths. Panchromatic cathodoluminescence (CL) was used to image threading dislocations as dark spots in the CL image, enabling the determination of areal density and spatial distribution of threading dislocations in $Al_{0.3}Ga_{0.7}N$ epilayers overgrown on GaN substrates. CL images were taken using a MonoCL system from Gatan that is installed on an FEI NanoSEM 200 scanning electron microscope (SEM). An accelerating voltage of 3 kV and a beam current of 3.6 nA were selected to minimize excitation volume while still providing sufficient signal and contrast to clearly resolve dislocations.

2.1.1. AlGaN Material Growth - Laser Heterostructures

All group-III nitride epilayers were grown by metal-organic vapor phase epitaxy (MOVPE) in a Veeco D-125 reactor at 75 torr. Conventional precursors, including trimethylgallium (TMGa), trimethylaluminum (TMAl), and ammonia, were used to grow $Al_xGa_{1-x}N$ alloys, while silane was used

for n-type doping and bis(cyclopentadienyl)magnesium(II) (i.e. magnesocene) for the p-type doping. Nitrogen and hydrogen were used as carrier gases.

Optimization of LD structures to maximize electroluminescence was conducted using heterostructures grown on sapphire substrates. This not only reduces cost by eliminating the use of expensive GaN substrates but more importantly, allows for relatively quick and quantifiable electroluminescence measurements by avoiding optical absorption of GaN substrates. For growth on sapphire, a 1.5 um thick AlN epilayer was grown on a 1.3 mm-thick, c-plane miscut 0.2° toward m, sapphire substrate. These substrates are ~3 times thicker than typical 2-inch-diameter sapphire (0.43 mm) and greatly reduce wafer bow and cracking of thick epilayers [8].

Following the AlN epilayer, a Si-doped (N_o = 1 x10^{18} cm^{-3}), 0.75 μm-thick $Al_{0.3}Ga_{0.7}N$ epilayer was grown to facilitate the transition between 3D and 2D growth. This strain driven 3D-to-2D growth process relaxes the $Al_{0.3}Ga_{0.7}N$ epilayer to approximately 80-85% of the unstrained lattice constant and achieves a threading dislocation density of 1-2 x 10^9 cm^{-2} based on x-ray diffraction measurements [9]. Next, a 1.7-μm-thick, heavily-doped (N_o = 7 x 10^{18} cm^{-3}), n-type $Al_{0.3}Ga_{0.7}N$ current spreading and contact layer. The $Al_{0.3}Ga_{0.7}N$ epilayer was grown at 1050 °C, the same pyrometer temperature used for the growth of GaN, using a group-III molar flow rate of 60 μmoles/min, and an Al/group-III ratio of 0.34. The growth rate was 0.6 μm/hr as determined by *in-situ* reflectance. Growth conditions and especially temperature are critical for minimizing the density of carrier-compensating defects in Si-doped AlGaN epilayers [10, 11]. Hall effect measurements of $Al_{0.3}Ga_{0.7}N$ epilayer calibration contact layers showed an electron concentration of 7 x 10^{18} cm^{-3} with a mobility of 81 cm^2/Vs and less heavily doped calibration layers yielded electron concentrations of 5-7 x 10^{16} cm^{-3} with a mobility of 123-150 cm^2/Vs. No residual conduction was observed in AlGaN test layers that were not intentionally doped with Si or Mg.

The quantum well of the optical active region consisted of a 15 to 25 Å thick GaN layer surrounded by an $Al_xGa_{1-x}N$ barrier layer where the thickness (35-50 Å) and composition ($0.18 < x_{al} < 0.23$) of the barrier layer depended on the emitter design. The quantum well structures were grown under conditions that were similar to the underlying n-type buffer while the Al/Group III ratio was adjusted to achieve the target composition for the barrier layer.

2.1.2. AlGaN Material Growth – Polarization p-type Doping for Optical Cladding

In typical AlGaN laser designs, hole injection and optical confinement are achieved with impurity doped p-type cladding. Unfortunately, acceptor impurities have a very large activation energy in $Al_xGa_{1-x}N$ alloys resulting in epilayers with poor hole conductivity. While Mg acceptors have the lowest activation for p-type impurity dopants in $Al_xGa_{1-x}N$ alloys, the acceptor activation energy is over 300 meV for $Al_{0.3}Ga_{0.7}N$ epilayers. Figure 2-11 (left) shows the room temperature resistivity measured by Hall effect as a function of Al compositions for $Al_xGa_{1-x}N$ epilayers doped with Mg at a concentration of ~3x10^{19} cm^{-3}. This Mg level was found to minimize hole resistivity for both GaN and $Al_{0.3}Ga_{0.7}N$ epilayers, Figure 2-11 (right). We also note that the resistivity becomes more strongly dependent on Mg concentration as the Al mole fraction increases. We find that for epilayers with Al mole fractions near 0.3, the resistivity is typically between 3 to 6 ohm-cm for the best material which is 3 to 6x higher than measured for common p-GaN (~ 1 ohm-cm). Consequently, this is a significant reason that UV laser diodes employing Mg impurity doped $Al_{0.3}Ga_{0.7}N$ claddings suffer high operating voltages and excessive ohmic heating compared to blue (InGaN) laser diodes using p-GaN epilayers for optical claddings.

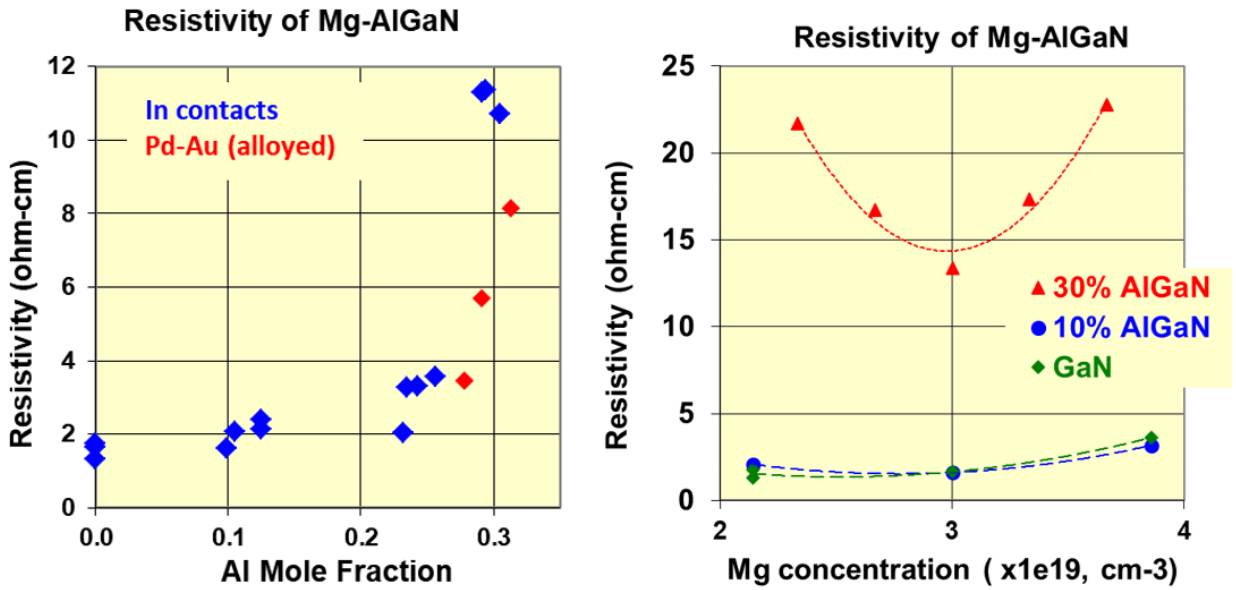

Figure 2-11. Room temperature resistivity measured by Hall effect as a function of Al compositions for $Al_xGa_{1-x}N$ epilayers doped with Mg at a concentration of 3x 10^{19} cm^{-3} (left) and as a function of Mg concentration for various alloy compositions and GaN (right). The minimum resistive is achieved for a Mg concentration 3x10^{19} cm^{-3}.

To increase p-type conductivity, we utilized polarization fields that are intrinsic to compositionally graded, wurtzite AlGaN alloys grown on (0001) c-plane to field ionize Mg acceptors. This essentially renders hole activation insensitive to thermal energy and allows for much higher p-type conductivity. For the metal polar $Al_xGa_{1-x}N$ epilayers used in the work, we developed p-type optical claddings where the Al mole fraction linearly graded from 0.60 down to 0.30 over 0.45 μm while the Mg molar flux was constant. The p-cladding was contacted by linearly grading the Al mole fraction down to GaN over 300 Å. The structure was completed with a p-GaN contact layer was grown.

To assess the effectiveness of p-type doping employing polarization fields, Hall measurements were made on a series of structures that are similar to the p-type optical cladding and were grown with different concentrations of Mg, example shown in Figure 2-12. The structure was repeated for Mg concentrations ranging from 1x10^{18} cm^{-3} to 6x10^{19} cm^{-3}. While the AlGaN test structure was designed to study optical absorption loss with Mg concentration in the graded layer, subsequent Hall measurements show the structure was also useful for determining carrier transport. Additionally, Secondary Ion Mass Spectroscopy (SIMS) measurements of Mg doped $Al_{0.3}Ga_{0.7}N$ epilayer test structures showed that the Mg concentration was linear with Mg flux from the detection level ~ 2x10^{17} cm^{-3} to 4x10^{19} cm^{-3} suggesting that Mg incorporation in AlGaN epilayers at these lower compositions is well behaved. Figure 2-13 shows the room temperature resistivity from Hall measurements of the polarization p-doped cladding structures as a function of Mg concentration. We see that the resistivity decreases with decreasing Mg concentration to the point that it is like that of simple p-GaN layers when the Mg concentration is 1-2x10^{18} cm^{-3}. The ~ 1 ohm-cm resistivity for the polarization doped cladding structures is roughly 3-6x lower than what we typically measure for impurity doped $Al_{0.3}Ga_{0.7}N$ epilayers and yet the average Al composition of the graded structure is much higher. Even more remarkable is that the maximum hole conductivity is achieved at a Mg concentration roughly 15 to 40x lower than is optimum for impurity doped $Al_{0.3}Ga_{0.7}N$ epilayers. At a Mg concentration of only 1-2x10^{18} cm^{-3}, impurity doped GaN or $Al_{0.3}Ga_{0.7}N$ epilayers would be extremely resistive and difficult to measure.

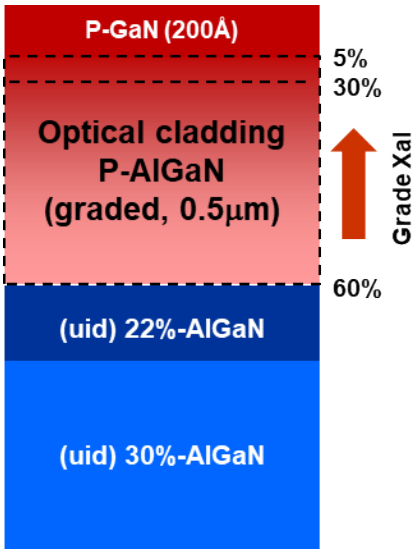

Figure 2-12. Epi-structure for Hall measurements that are similar to polarization doped p-type optical claddings used in laser diodes. The structure was repeated for Mg concentrations ranging from 1x10^{18} cm^{-3} to 6x10^{19} cm^{-3}.

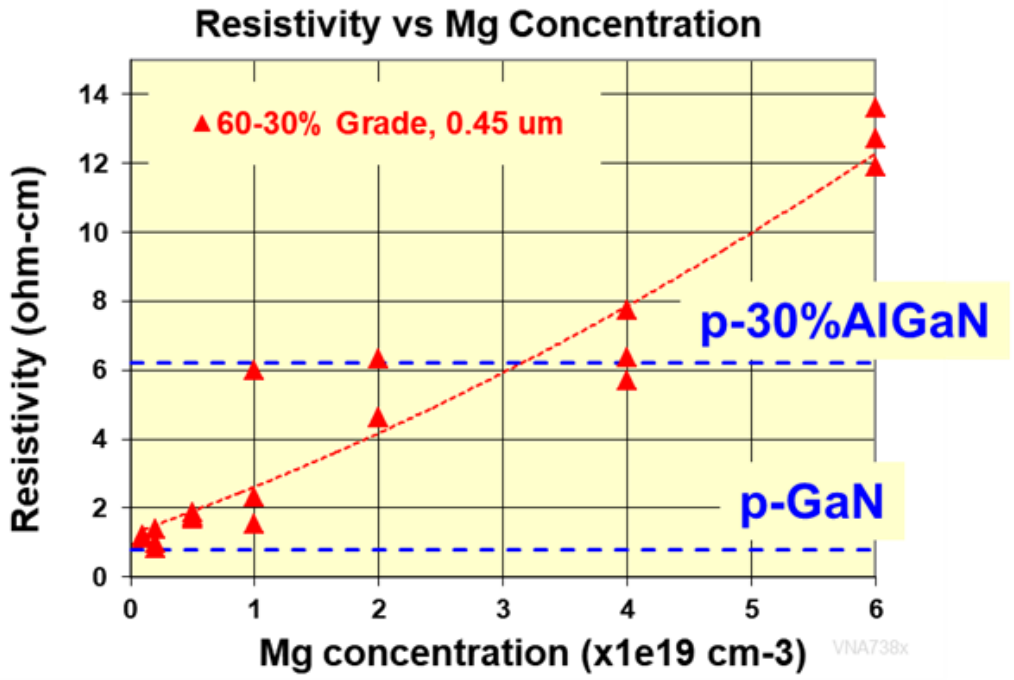

Figure 2-13. Room temperature resistivity from Hall measurements of the polarization p-doped cladding structures (Figure 2-12) as a function of Mg concentration. The resistivity of the AlGaN graded structures matches that for p-GaN epilayers when the Mg concentrations reaches -2x10^{18} cm^{-3}. Blue dashed lines are the typical resistivities measured in Mg impurity doped $Al_{0.3}Ga_{0.7}N$ and GaN layers when doped with at an optimum Mg level of ~ 3x10^{19} cm^{-3}.

Figure 2-14 shows the room temperature hole concentration and Mg concentration as measured by SIMS with Mg dopant source flux. As is the case with resistivity, the hole concentration increases

by over an order of magnitude with a corresponding change in Mg concentration. A hole concentration of 0.8-1.2x10^{18} cm^{-3} was measured in structures where the Mg concentration was 1 or 2x10^{18} cm^{-3}. This indicates nearly 100% ionization of Mg acceptors in this high Al graded structure which is in great contrast to the ~ 1-2% ionization rate for Mg doped GaN. The great reduction in resistivity with over an order of magnitude lower Mg and the near 100% ionization of Mg acceptors strongly indicates that acceptor ionization is occurring by means other than thermal activation and is indeed consistent with ionization by polarization files in the crystal structure.

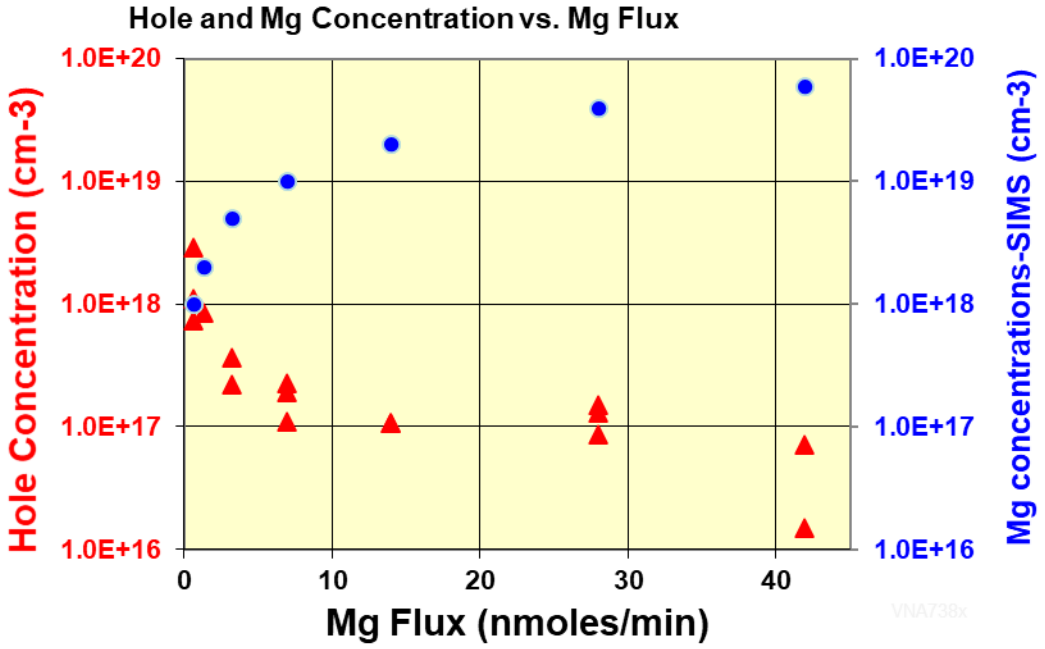

Figure 2-14. Room temperature hole concentration and Mg concentration as measured by SIMS with Mg dopant source flux. Nearly 100% ionization of Mg acceptors is observed in graded AlGaN structures with a Mg concentration of 1 or 2x10^{18} cm^{-3} which illustrates the effectiveness of polarization fields for ionization of Mg acceptors.

2.1.3. AlGaN Material Growth – Overgrowth of Patterned, Conductive GaN Substrates

AlGaN based laser diodes emitting at UV wavelengths cannot be grown pseudomorphically on low-defect GaN substrates using a conventional epitaxial growth process. Consequently, lasers at these wavelengths require the use of conductive, non-native substrates and effective methods to achieve low dislocation density while managing epilayer tensile strain. Sandia has innovated an approach of AlGaN overgrowth of patterned $Al_xGa_{1-x}N$ epilayers on sapphire templates. The major innovation is the use of submicron-wide-mesas on a 2 μm pitch [8, 12]. $Al_{0.3}Ga_{0.7}N$ overgrowth of these narrow features yields spatially uniform threading dislocations density (TDD) of 2-3 x 10^8 cm^{-2}. Using this process, Sandia has demonstrated similarly low TDDs over the entire range of $Al_xGa_{1-x}N$ alloy compositions and enabled Sandia to be one of several groups world-wide to demonstrate AlGaN-based UV lasers.

Generation I (parallel strips): We modified the patterning and overgrowth process that was previously used for $Al_{0.3}Ga_{0.7}N$ on sapphire [8] to conductive GaN substrates in order to grow laser heterostructures that are vertically conducing. Instead of patterning $Al_xGa_{1-x}N$ epilayers on sapphire,

commercial, free-standing GaN substrates where patterned with parallel mesas and trenches across the entire 2-inch diameter wafer. To develop an $Al_{0.3}Ga_{0.7}N$ overgrowth process on GaN substrates, a series of GaN substrates were prepared with parallel strips aligned parallel to either the a-plane or m-plane of the substrate, as shown in Figure 2-15. Patterns consisted of a range of strip widths (mesas) and a range of separations (trenches) between strips. Additionally, patterns with different trench depths were investigated. Conventional contact lithography and etching were used to open windows in a blanket covering of SiN_x mask. An inductively coupled plasma (ICP) was used to etch trenches in the underlying GaN substrate. After removal of the SiN_x etch mask, a thin n-GaN buffer layer was grown followed by 5 to 8 μm of Si-doped (1-3x10^{18} cm^{-3}) $Al_{0.3}Ga_{0.7}N$ on the patterned GaN substrate using growth conditions similar to those used to planarize $Al_{0.3}Ga_{0.7}N$ epilayers overgrown on patterned $Al_{0.3}Ga_{0.7}N$ on sapphire.

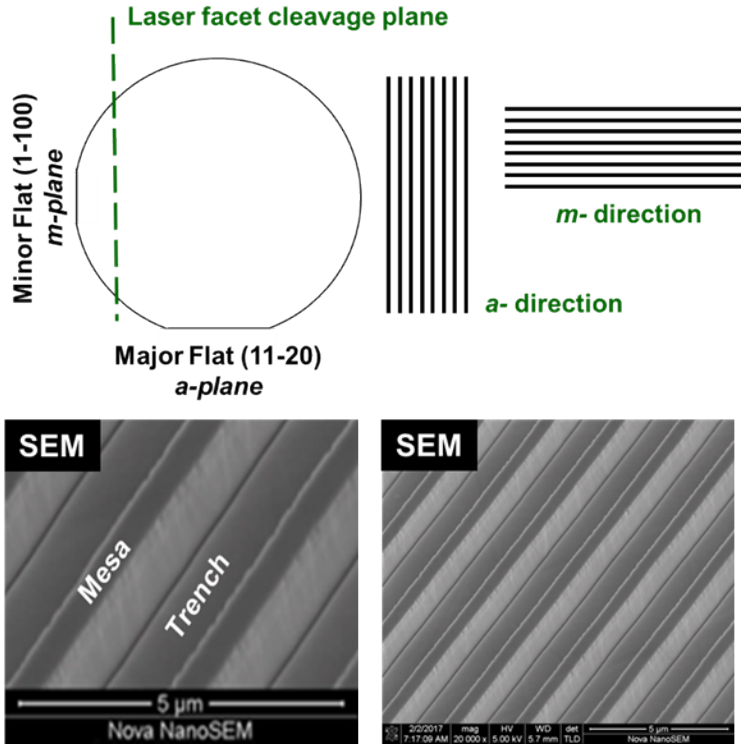

Figure 2-15. GaN substrates were prepared with parallel strips aligned parallel to either the a-plane or m-plane of the substrate (top). Secondary Electron Microscopy images show pattern of parallel strips etched into a free-standing GaN substrate prior to epitaxial growth (bottom).

Fully coalesced, pit-free, $Al_{0.3}Ga_{0.7}N$ epilayers, Figure 2-16, were achieved when grown on GaN substrates patterned with nominally 1 μm wide strips aligned in the a-direction and separated by 1 μm wide trenches which were etched 0.6 μm deep. While not clear in the micrograph in Figure 2-16, the $Al_{0.3}$ $Ga_{0.7}N$ surface had macro-steps roughly aligned parallel to the a-direction. AFM images (Figure 2-17) show the macro-step features typically observed in overgrown $Al_{0.3}Ga_{0.7}N$ epilayers. We expect that the macro-step can be minimized by optimizing growth conditions and surface miscut of the starting GaN substrate. Figure 2-17 also shows well-resolved, parallel atomic steps present over the surface of the overgrown $Al_{0.3}Ga_{0.7}N$ epilayer and furthermore, the overgrown AlGaN layer has no morphological signatures of the underling etched pattern consistent with a device quality $Al_{0.3}Ga_{0.7}N$ epilayer suitable for fabricating UV laser diodes.

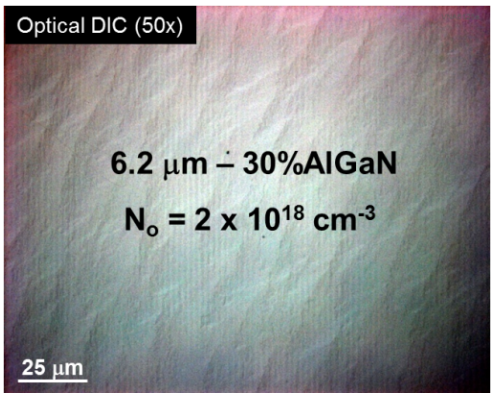

Figure 2-16. A Nomarski differential contrast micrograph showing a fully coalesced, Si-doped $Al_{0.3}Ga_{0.7}N$ epilayer grown on a conductive, GaN substrate patterned with parallel mesas separated by etched trenches.

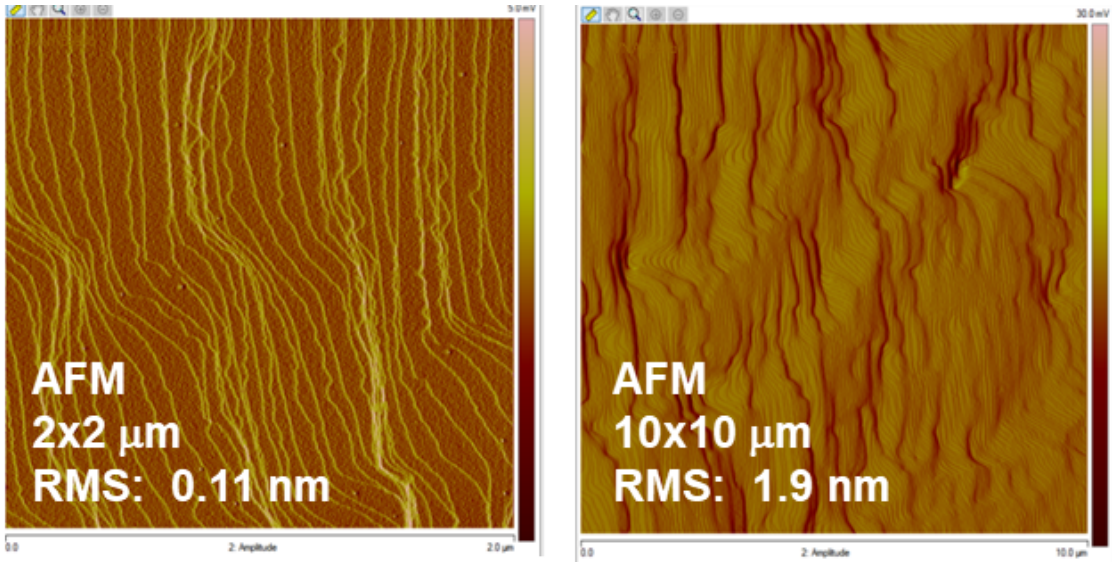

Figure 2-17. Atomic Force Microscopy images (phase contrast) show macro-step bunching of the surface of a 6-μm thick, n-type, $Al_{0.3}Ga_{0.7}N$ epilayer grown on a GaN substrate patterned with parallel mesas separated by etched trenches.

As was the case of $Al_xGa_{1-x}N$ overgrowth of patterned $Al_xGa_{1-x}N$ on sapphire templates, the use of submicron wide mesa strips facilitates the reduction of threading dislocations over the narrow strip resulting in a random distribution of threading dislocations over the $Al_xGa_{1-x}N$ surface. Threading dislocations that are propagating normal to the surface of the mesa experience an image force since they are near a free surface before planarization and consequently incline from normal. This both reduces their density over the mesa as well as increases the probability they will annihilate by interaction with another dislocation. This eliminates the high dislocation density observed over wider strips that compel alignment of laser strips to the low dislocation regions between strips.

Figure 2-18 show panchromatic cathodoluminescence images from quantum wells regrown on an 8-μm thick $Al_{0.3}Ga_{0.7}N$ epilayer grown on a GaN substrate patterned with submicron wide, parallel mesas separated by etched trenches on a 2 μm pitch. The dark spots in the CL images indicate the presence of non-radiative recombination of electron and holes at the location of a threading

dislocation. The dislocation density determined by CL is estimated to be 5-8x10^8 cm^{-2}. We see that the density of dark spots over the surface is largely random and is not associated with the underling patterned etched in the GaN substrate. There is some congregating of dark spots along the edge of macro-steps observed on the surface. Hence, efforts to reduce the formation of macro-steps should result in a lower density of threading dislocations.

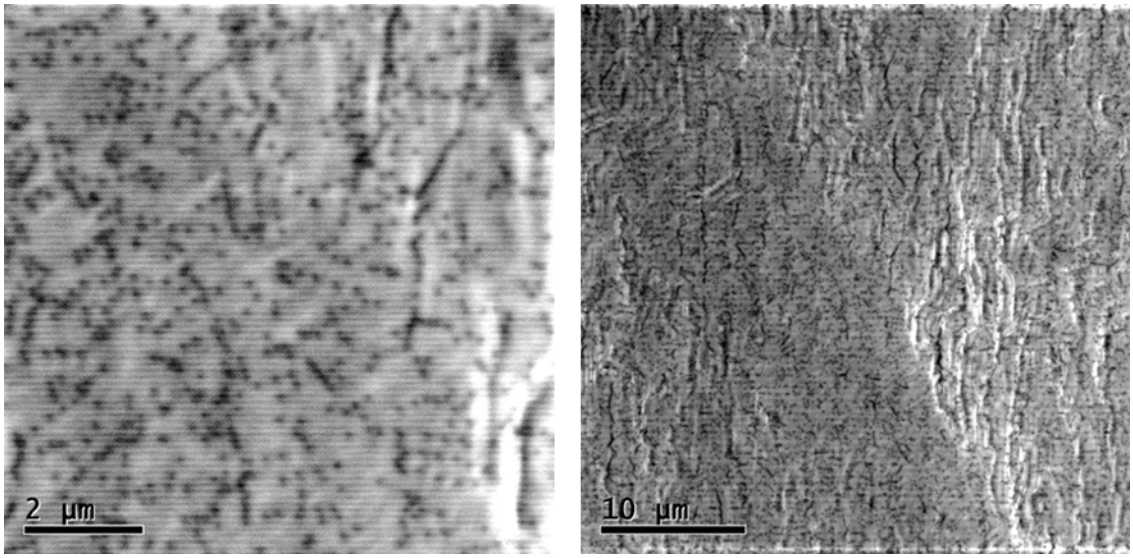

Figure 2-18. Panchromatic cathodoluminescence images from quantum wells regrown on a 8-μm thick $Al_{0.3}Ga_{0.7}N$ epilayer grown on a GaN substrate patterned with sub-micron wide, parallel mesas separated by etched trenches on a 2 μm pitch.

Templates like that shown in Figure 2-16 were used for subsequent regrowth of laser heterostructures. However, random cracks propagating perpendicular to the mesa strips was observed in overgrown $Al_{0.3}Ga_{0.7}N$ epilayers and laser heterostructures. The density of cracks varied greatly with some wafers being useless for future growth of laser heterostructures while other wafers had a lower density of cracks and could be used for the growth laser heterostructures. The density of cracks in the <11-20>AlN direction (i.e. parallel to the major flat) can be reduced to some extent by fine tuning Si doping, thickness of the AlGaN overgrowth, and parameters of the pattern. However, the crack density still varied substantially from wafer to wafer, limiting the yield of wafers for device processing. Part of the cracking is believed to be related to large degree of wafer bow that develops due to different lattice constant between the $Al_xGa_{1-x}N$ overgrowth layer and GaN substrate. We also suspect that the 1-dimensional aspect of the etch pattern did not effectively relieve crystal strain along the strip leading to cracking perpendicular to the strip. Hence, we investigated etching 2-dimensional patterns into the starting GaN substrate.

Generation II (2-dimensional patterning): We investigated etching 2-dimensional patterns into free-standing GaN substrates as way to relieve strain in orthogonal directions to eliminate cracking frequently observed in $Al_{0.3}Ga_{0.7}N$ grown on 1-dimensional, parallel strip patterning. As was done for parallel strips, we investigated different patterns, their alignment to m- and a- crystal planes and, etch depths and spacing between 2D pattern mesas. $Al_{0.3}Ga_{0.7}N$ overgrowths were done on half wafers cleaved from 2-inch diameter free standing GaN substrates. Using the same growth conditions for $Al_{0.3}Ga_{0.7}N$ overgrowth of parallel strips, fully coalesced, pit free $Al_{0.3}Ga_{0.7}N$ epilayers were achieved on 2D patterned GaN substrates (Figure 2-19). Most importantly, cracking was greatly reduced with 2D patterning offering the potential for good yields of laser diodes. Macro-steps were

observed aligned in both the a- and m-directions that we expect can be reduced with optimization of the mis-cut of the GaN wafer and $Al_{0.3}Ga_{0.7}N$ growth conditions. A series of vertically conducting laser heterostructures were grown on Si-doped $Al_{0.3}Ga_{0.7}N$ templates prepared in this manner.

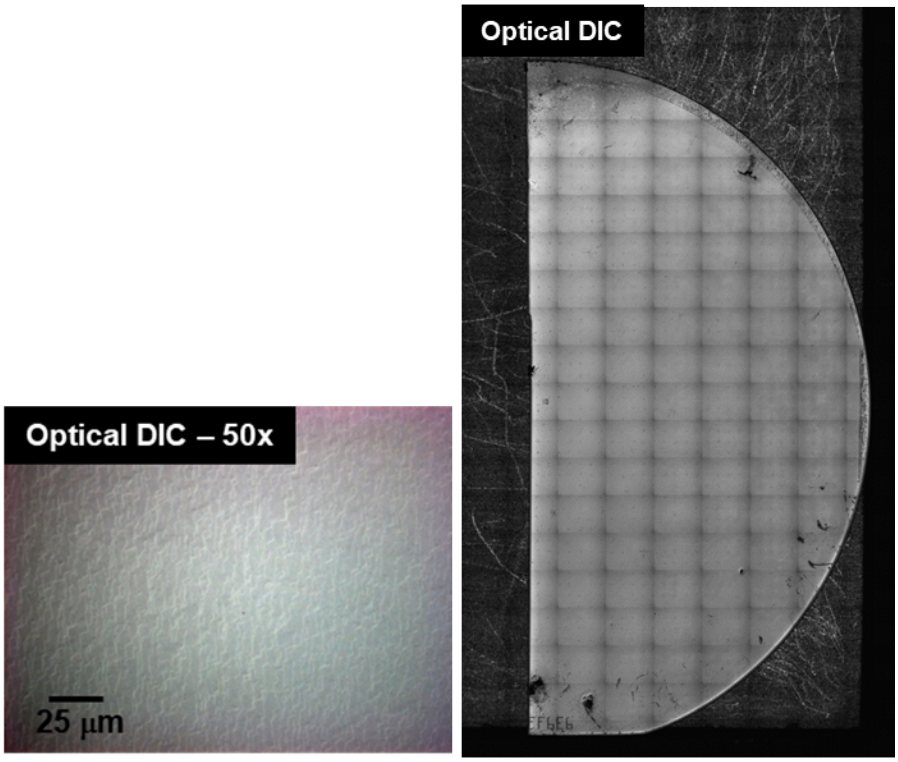

Figure 2-19. A Nomarski differential contrast micrograph showing a fully coalesced and planarized, Si-doped $Al_{0.3}Ga_{0.7}N$ epilayer grown on a half of a 2-inch diameter GaN substrate with an etched 2-dimensional pattern.

2.2. Fabrication

The fabrication of devices included circular transfer length method (TLM), electroluminescence quick-test devices, large-area diodes, and ridge waveguide diodes. Our process took the approach of depositing the p-type metal as a first step in order to make the metal-semiconductor contact as clean as possible. We confirmed the effectiveness of this process through TLM device structures and measurements. There was a good deal of effort to establish a self-aligned ridge waveguide process and several process advancements were established to overcome process roadblocks.

2.2.1. Process revision 1

Prior Sandia UV laser development involved AlGaN epitaxy on insulating sapphire substrates that did not share a common cleavage plane with the AlGaN epitaxial material. This process therefore involved etched facets and a geometry with both contacts on the top side of the wafer. Furthermore, while the existing process included plasma etching to form ridge waveguide structures, the process was not optimized for achieving very narrow ridges (~ 1.5 μm) for better modal confinement. This LDRD project moved beyond sapphire substrates to electrically conductive GaN substrates, offering the advantages of cleaved facets, direct vertical current injection (contacts on top and bottom of the device) and better thermal performance. Work in this project included the development of a new self-aligned ridge waveguide process to realize narrow-ridge devices with vertical current injection.

In Figure 2-20, we show a process flow for the self-aligned ridge waveguide (RWG) process. The process starts with a rapid thermal anneal to activate p-type dopants (not shown). This step is followed by photolithography to prepare for a lift-off process and sequential e-beam evaporation of the Pd/Au p-type contact metals and a SiO_2 hard mask. After lift-off, the sample has stripes of a metal/dielectric stack with widths ranging from ~1 μm to 10 μm. Inductively coupled plasma (ICP) etching with a $BCl_3/Cl_2/Ar$ chemistry enabled etching of ridges through most of the p-type cladding of the laser heterostructure and was followed by removal of the SiO_2 hard mask with a buffered oxide etch (BOE). This "self-aligned" RWG process enabled ridge widths as narrow as ~1.5 μm and full p-contact coverage of these ridges, an improvement over our prior process.

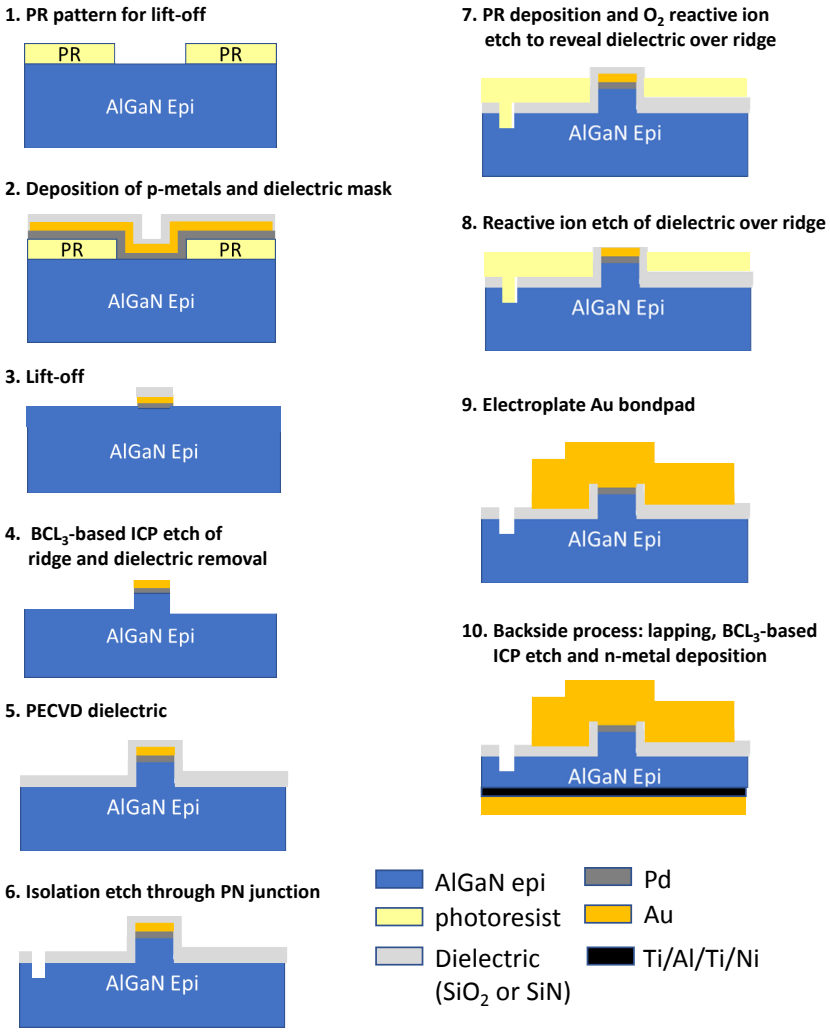

Figure 2-20. Process flow for self-aligned ridge waveguide laser process (schematics not to scale).

Plasma-enhanced chemical vapor deposition (PECVD) is then employed to deposit a new SiO_2 (or SiN) hard mask. Neighboring devices are electrically isolated by first photoresist (PR) patterning and etching an opening in the dielectric. This dielectric is then used as a mask for BCl_3-based ICP etching through the p-n junction of the heterostructure. The next step is a "via' process to enable etching away of the dielectric coating only over the ridges, allowing access to the p-type metals while keeping

dielectric in the field and on the ridge sidewalls. This is accomplished with deposition of a thick PR over the wafer and then a carefully timed oxygen reactive ion etch that opens the PR only over the ridges. Reactive ion etching (RIE) is then performed to remove the dielectric over the ridges and reveal the p-type contact metals.

A Ti/Au seed metal is then sputtered, patterned with PR, and followed by electroplating of a ~ 2 μm thick Au p-bond pad metal. Backside device processing involved dicing out individual die, sub-mounting several die on a Si carrier wafer using crystal bond, and lapping the die with a boron carbide slurry to achieve a final thickness of ≤ 100 μm. To remove polishing damage, a BCl_3-based plasma etch is performed on the lapped GaN surface of sub-mounted die, removing approximately 0.5 μm, of material. E-beam evaporation of a Ti/Al/Ti/Ni/Au contact metal completes the back-side processing. Individual die are removed from the Si carrier, cleaned and cleaved into individual laser bars with lengths of ~ 0.6-1.2 mm.

2.2.2. Process revision 2

After running the original process flow, we identified a primary failure mode. This failure mode involved a parasitic diode short that occurred under high current injection conditions. This failure mode was not recoverable and was observed as a sudden drop of the voltage at a given current and subsequent I-V sweeps showed a below bandgap turn-on. Further analysis showed that epitaxial defects under the pad metal were the primary source of the short. Previous projects had identified a nano-pipe type defect that is manifested as a very high aspect-ratio pit. The dielectric deposition process used in the original process, we speculate, was not able to bridge the nano-pipe gap allowing metal to reach the underlying semiconductor material. This high resistance metal-semiconductor contact was heated under high current and eventually resulted in a decreased shunt resistance and current then was able to bypass the active region of the laser structure.

Using this knowledge, we devised a new process that uses a spin-on polymer to aid in bridging the high-aspect-ratio nano-pipe defects present in the field. In this new process we used the dry-etch Benzocyclobutene (BCB) formulation to coat the wafer prior to a blanket etch-back process to expose the top of the ridge waveguides. This new process has two main benefits, first to coat the nano-pipe defects and prevent the pad metal from shorting to the underlying semiconductor, and second, to planarize over the ridge waveguides, representative process shown in Figure 2-21. This planarization greatly helped to ease the etch-back process over narrow ridges, eliminating difficult and time-consuming backside exposure process that was developed in the original process flow. The blanket etch-back is an un-patterned uniform dry etch of the BCB polymer. Since the BCB is very good at planarizing the surface morphology, we can expose the top of the ridge waveguide before the field BCB is fully etched as shown in Figure 2-22.

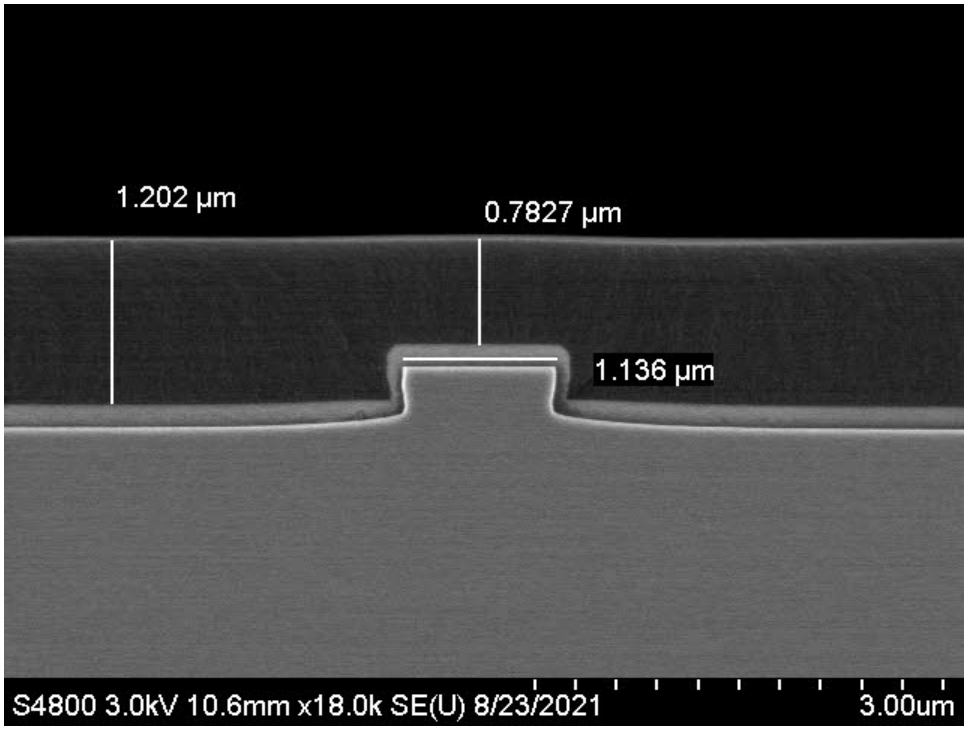

Figure 2-21. Cross-section of a planarization process showing the effectiveness of dry-etch BCB over ridge waveguides.

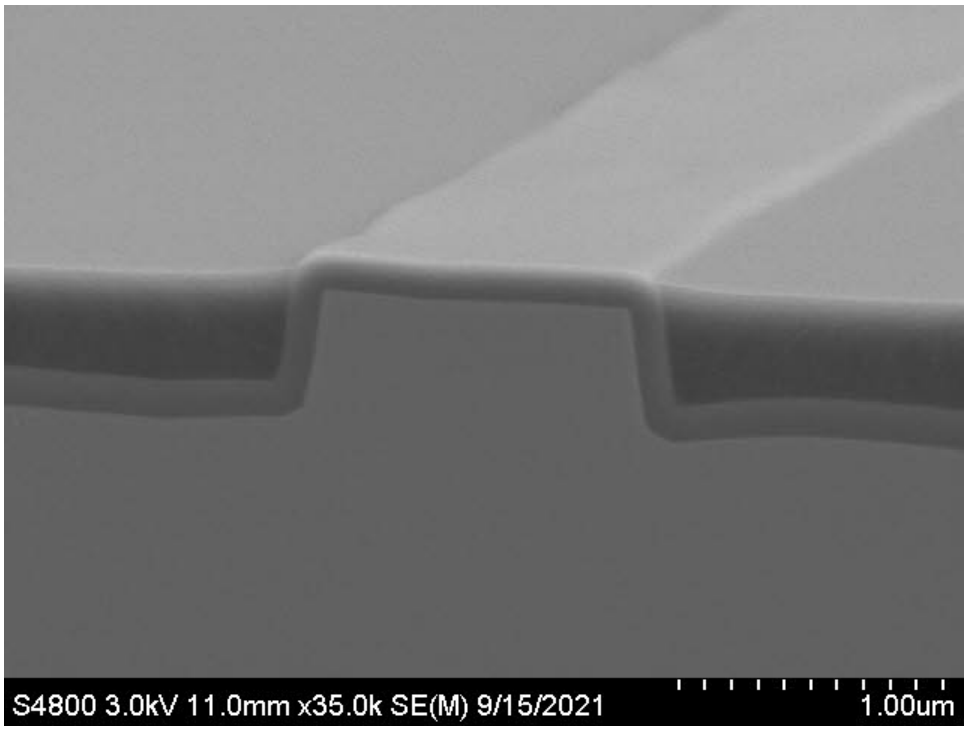

Figure 2-22. Blanket etched BCB showing the top of the ridge waveguide exposed and the field still covered in BCB.

We believe that this new process will be effective in preventing the main failure mode of a shunt resistance forming between the pad metal and underlying semiconductor. This process is already being leveraged by other projects and will continue to be utilized in the future.

2.3. Device Data

The accumulation of device data was certainly stifled by the COVID-19 pandemic, nevertheless we were able to extract several key device metrics during the project. Although we did not yet achieve a device was able to reach a laser threshold, we did make significant strides in several areas, including electroluminescence testing, waveguide test and measurement, contact and sheet resistance, and vertical diode test and measurement.

2.3.1. Waveguides

Optical waveguide loss in polarization-doped AlGaN laser structures grown on a sapphire substrate was measured using evanescent wave light coupling. Polarization-doped laser structures are expected to have lower internal loss since less Mg doping is required to achieve the same p-layer conductivity. Waveguide loss can be measured using evanescent coupling without extensive sample preparation and without knowledge of the coupling loss.

The basic evanescent coupling experimental setup is shown in the diagram in. A transparent prism Figure 2-23 is placed in near-contact (<100 nm away) to the top surface of an AlGaN waveguide. Light is totally internally reflected at the air-prism interface if the angle of incidence θ is larger than the critical angle. Without the presence of the AlGaN waveguide, a standing wave is formed inside the prism and an exponentially decaying evanescent field extends outward from the prism-air interface. If the AlGaN waveguide is placed close enough to the bottom surface of the prism, the evanescent field can couple across the air gap and into the waveguide. The refractive index of the prism must be larger than the waveguide refractive index therefore a TiO_2 (rutile phase) prism is often chosen because of its high refractive index ($n > 3.0$ for $\lambda < 500$ nm).

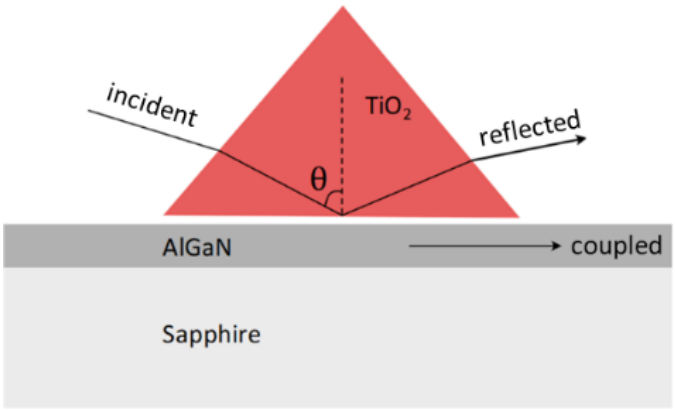

Figure 2-23. Simplified diagram of evanescent wave coupling into AlGaN waveguide.

The waveguide loss is extracted by measuring the intensity of the light that is scattered from the waveguide as the coupled wave propagates down the waveguide. This is often done by using a scanning fiber optic probe or by imaging the scattered light with a camera. The intensity of the scattered light is equal to the intensity of the light in the waveguide within a multiplicative factor. We can expect that

the intensity of the scattered light will have the form $I_s = I_0 \exp(-\alpha x)$ where α is the waveguide loss coefficient and x is the distance along the waveguide. The waveguide loss coefficient is extracted by plotting the logarithm of the scattered light intensity as a function of distance along the waveguide. Both absorption and scattering loss comprise the waveguide loss coefficient. It is not possible, for example, to extract the absorption loss if scattering loss is the dominant loss mechanism.

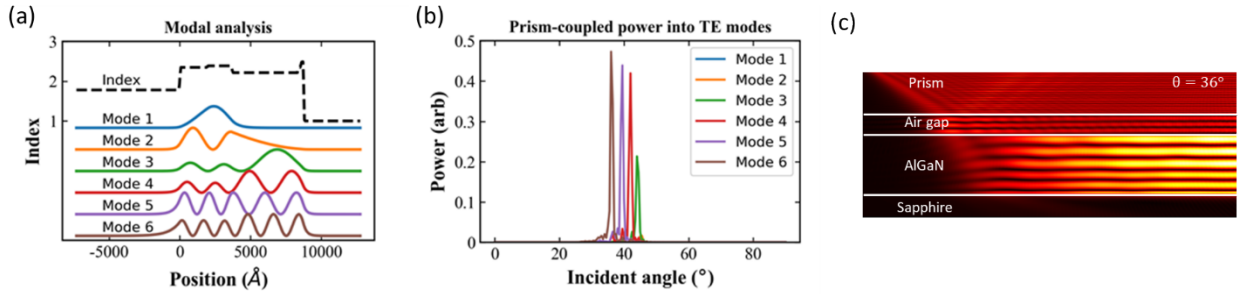

Figure 2-24. (a) An overlay plot of the refractive index as a function of distance and the first six supported modes in an example laser structure; (b) plot of the coupled power versus incidence angle; and (c) plot of electric-field for light coupled into the 6th mode.

Two-dimensional finite difference time domain (FDTD) modeling was used to study evanescent coupling in an AlGaN slab waveguide. Shown in Figure 2-24 (a) is the plot of the refractive index profile of an example AlGaN laser diode structure. Overlayed on the sample plot is the mode profile for the first 6 transverse-electric (TE) modes supported by this structure. The light intensity coupled into the waveguide from an incident monochromatic light (λ = 445 nm) plane wave was monitored as a function of the angle of incidence. As shown in Figure 2-24 (b), the power coupled into each TE mode can be changed by modifying the incidence angle; this is a consequence of phase matching between the propagating mode and incident light. As an example, the simulated electric-field is plotted in Figure 2-24 (c) for θ= 36° where light is mostly coupled into the 6th order mode.

We notice that minimal light is coupled into the fundamental mode for all angles of incidence. As can be seen in Figure 2-24 (a), the fundamental mode does not extend outside of the waveguide slab therefore we can expect that the evanescent light in the prism-air gap will only weakly couple to this mode. Edge-coupling must be used if it is necessary to couple to the fundamental mode. However, as we will show, scattering loss is dominant in the AlGaN waveguides grown on sapphire; we expect that scattering loss is only weakly dependent upon which mode is excited in the slab waveguide.

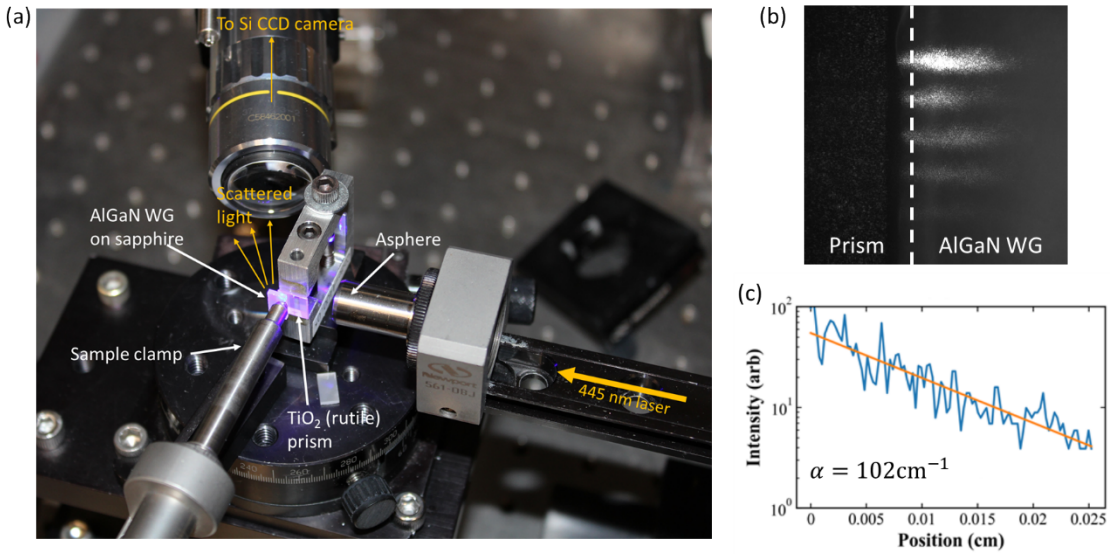

Figure 2-25. (a) Picture of the experimental apparatus used to measure waveguide loss; (b) image of light scattered from several broad-area waveguides; and (c) line-scan plot of the scattered light intensity.

The experimental apparatus used to measure waveguide loss is shown in Figure 2-25 (a). An Oxxius (λ = 445 nm) continuous-wave laser (not shown) was used to illuminate a TiO_2 prism that was clamped onto the surface of a chip containing several 50 μm wide broad-area AlGaN laser structures. Special AlGaN laser structures were grown on sapphire without n-type doping to evaluate the optical loss associated with p-type doping. Light that was scattered from the broad-area waveguides was collected with an infinity-corrected microscope objective and focused onto a TE-cooled silicon CCD camera. A typical image is shown in Figure 2-25 (b) which shows the light that was simultaneously scattered out of several different waveguides. A typical line-scan of the scattered light intensity is plotted in Figure 2-25 (c) where we extract a large waveguide loss of about 100 cm^{-1}. Several different waveguides across different chips were measured and we observed a waveguide loss range of 70 to 130 cm^{-1}.

This waveguide loss is substantially higher than expected from internal absorption alone therefore the loss likely comes from a different physical mechanism. AlGaN waveguides grown on sapphire have large dislocation densities (>10^9 cm^{-2}) which can introduce refractive index inhomogeneities that can scatter light. This was theoretically studied by Liau et al. [13] and later compared to experimental data by Tanaka et al [14]. Tanaka measured waveguide loss in $Al_{0.3}Ga_{0.7}N$ of ~100 cm^{-1} for dislocation density of ~2×10^9 cm^{-2} which closely matched the theoretical predictions. Our waveguides have similar loss and dislocation density therefore we conclude that the measured loss is mostly the result of high dislocation density. Therefore, it is not possible to directly extract the internal absorption loss for these samples. A future study of waveguide loss using epitaxy grown on GaN substrates should greatly reduce the dislocation density such that extraction of other loss mechanisms become evident. Nonetheless, this study highlights the need for low dislocation density to achieve lasers with reasonably low threshold gain and current.

2.3.2. *Electrical Measurements*

Part of the improvement that we anticipated when we started to investigate the polarization doping method for the p-type regions was an improvement of the p-type cladding resistance. In section 2.1.2, we showed the effect of a compositional grade on the hole concentration using Hall measurements. Here, we investigate the effect of the polarization doping on the electrical measurements using the circular transfer length method (TLM) [15]. Using this method, we can extract both the specific contact resistivity and the sheet resistance of the p-type contact and the p-cladding, respectively.

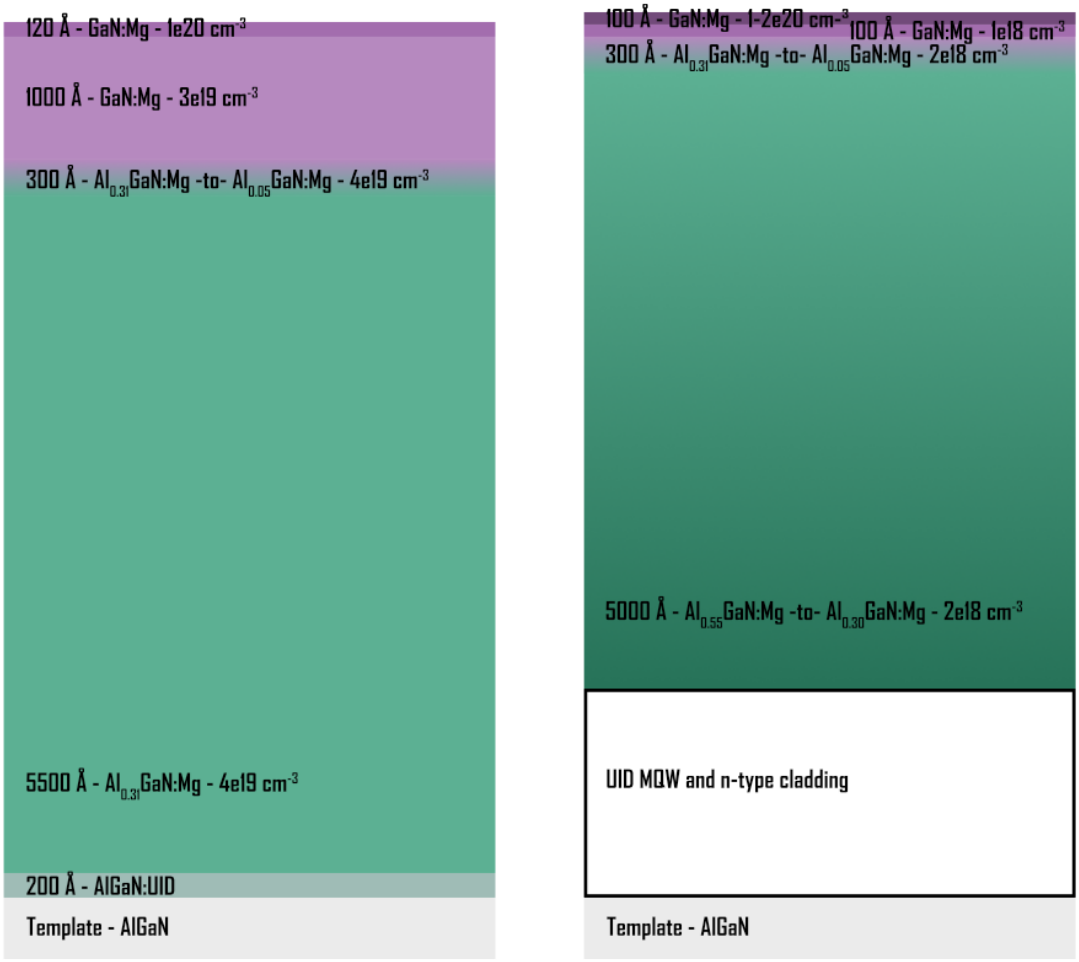

Figure 2-26. Device structures for the transfer length method electrical measurements. Left is the non-polarization doped structure; right is the polarization doped structure.

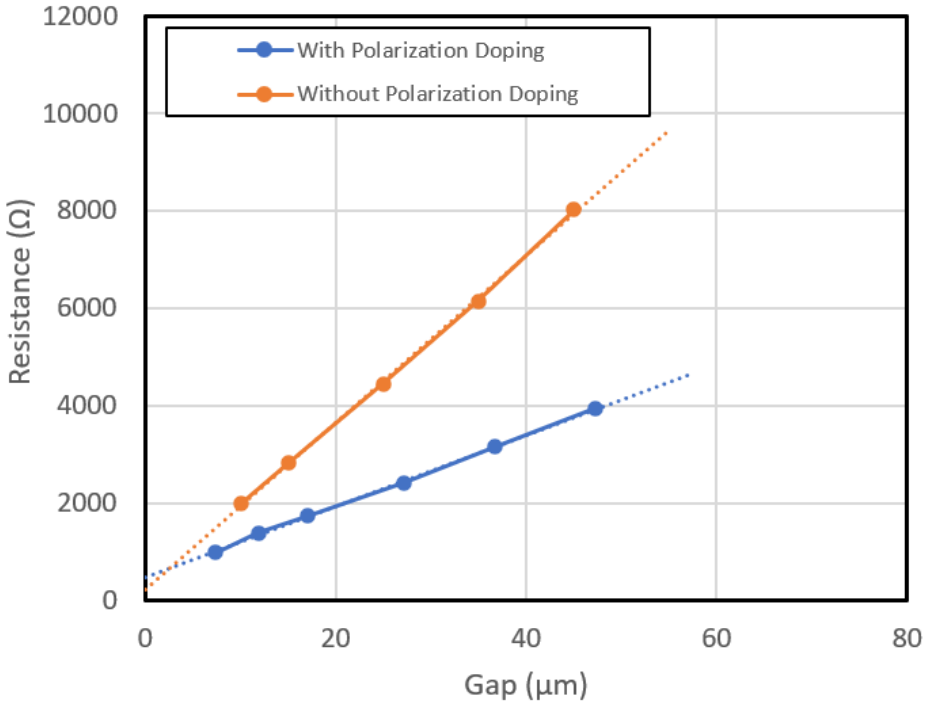

Figure 2-27. Transfer Length Method (TLM) for extracting the specific contact resistivity and the sheet resistance of the p-type cladding.

The structures shown in Figure 2-26 were used to compare the contact resistance and sheet resistance of p-cladding designs with and without polarization doping. As shown in the figure, the non-polarization doped structure has a thick, highly-doped AlGaN region followed by a relatively thin p-type GaN layers for making metal/semiconductor contact. Similarly, the polarization doped structure also has a relatively thick AlGaN region, except the AlGaN region is compositionally grated to achieve the desired polarization doping effect. Also of note is the difference in the Mg concentration in each of these samples, the non-graded/non-polarization doped structure has the AlGaN doped to a concentration of 4e19 cm^{-3} while the graded structure has a Mg concentration of only 2e18 cm^{-3}. Both these structures were used to fabricate circular TLM devices which were measured using Kelvin probing techniques. The results are plotted in Figure 2-27, which shows that the sample with polarization doping has a much lower sheet resistance as indicated by the lower slope of the line. Specifically, the sample with polarization doping achieved a sheet resistance of 34.8 kΩ/□ while the non-polarization doped sample demonstrated a sheet resistance of 80.8 kΩ/□. This improvement in the sheet resistance is remarkable, the sheet resistance is more than a factor of 2 lower for a Mg doping concentration that is more than an order of magnitude lower and a larger average Al-concentration in the sample. This shows the potential for polarization doping in electrically injected devices. The specific contact resistivity, on the other hand, was better in the non-polarization doped sample, 3e-4 Ω-cm^2 vs. 6e-3 Ω-cm^2. The difference in specific contact resistivity is not too surprising due to the differences in the structures near the surface where the metal contact is made.

2.3.3. *Diode Characterization*

Using the process described in 2.2.1 ridge waveguide diode devices were fabricated and I-V sweeps were used evaluate the diode behavior. Figure 2-28 (a) shows a typical I-V sweep from -8 V -to- 8 V plotted on a linear scale for a device with a length of 600 μm and ridge width of 3.5 μm. As shown in the figure the diode turns on at around 5 V and shows minimal reverse current. However, if we plot the reverse current on a nA scale, as shown in Figure 2-28, it becomes clear that at ~-5 V the reverse current begins to increase rapidly. There could be several reasons for this, one is generation current due to mid-gap trap states in the depletion region. Another possibility for this behavior is the turn-on of a reverse parasitic diode with a relatively large shunt resistance. Figure 2-29 also shows this behavior when the I-V is plotted on a semilog-y axis, the current is plotted as the absolute value and increases with increases with increasing reverse voltage. Also visible is change in slope at ~-5 V where the reverse current starts to increase at a more rapid pace, which is indicative of parasitic diode behavior.

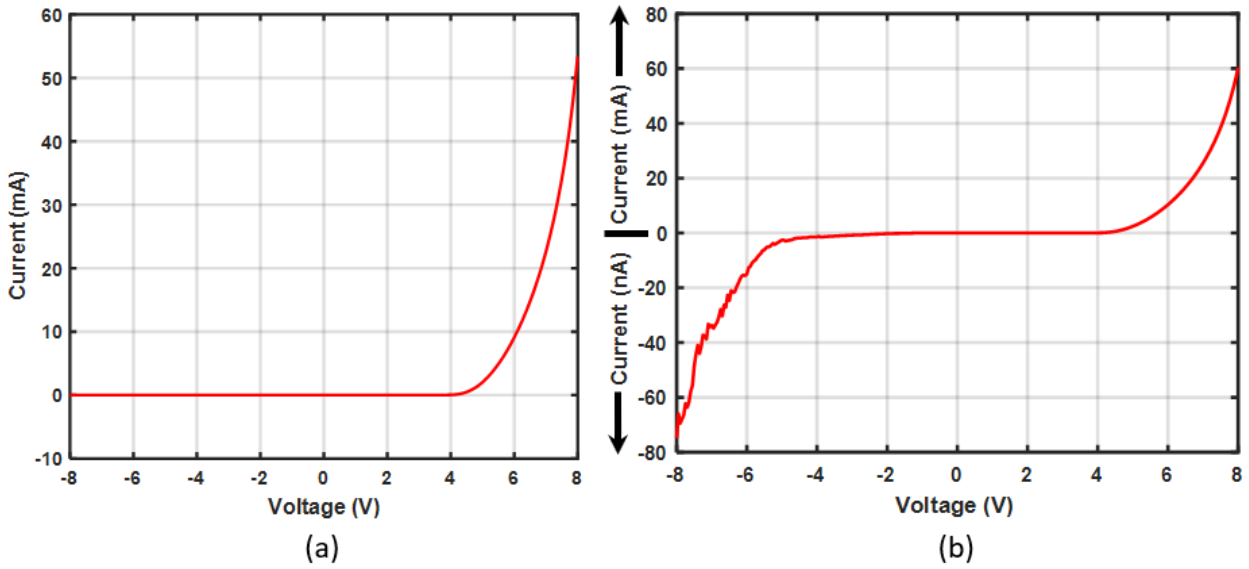

Figure 2-28. Current plotted as a function of voltage for device diode bar of 600 μm in length 3.5 μm in width. (a) shows the I-V in linear scale and (b) shows with magnified negative going current.

Turning attention to the forward voltage region of the semilog-y I-V sweep, Figure 2-29, one can see several slope changes which indicates some parasitic problems. There are two main causes for inflection points such as these, first is a parasitic shunt diode, the second is a parasitic shunt resistor. From the reverse voltage region current we can see that the current at -3 V is not the same as that at +3V, so we can say the major contributor for these inflection points is not due to shunt resistance, because a shunt resistor would show the same current in either forward or reverse bias. So, these inflection points are most likely due to parasitic shunt diode(s). These shunt diodes are likely formed between p-metal reaching the n-type cladding though unisolated material defects. These shunt diodes, under high current injection, can heat up and eventually short and create a resistive shunt. These defects are visually decorated, changing in shape and size once they reach the transition from diode to resistive shunt. In order to mitigate this parasitic shunt diode, we developed the modified process that uses BCB polymer to coat the etched field of the sample in order to isolate the material defects from the bond-pad metal. Device runs were started using this new process, but not completed before

the project period of performance had expired. We hope to use this new process in other related projects.

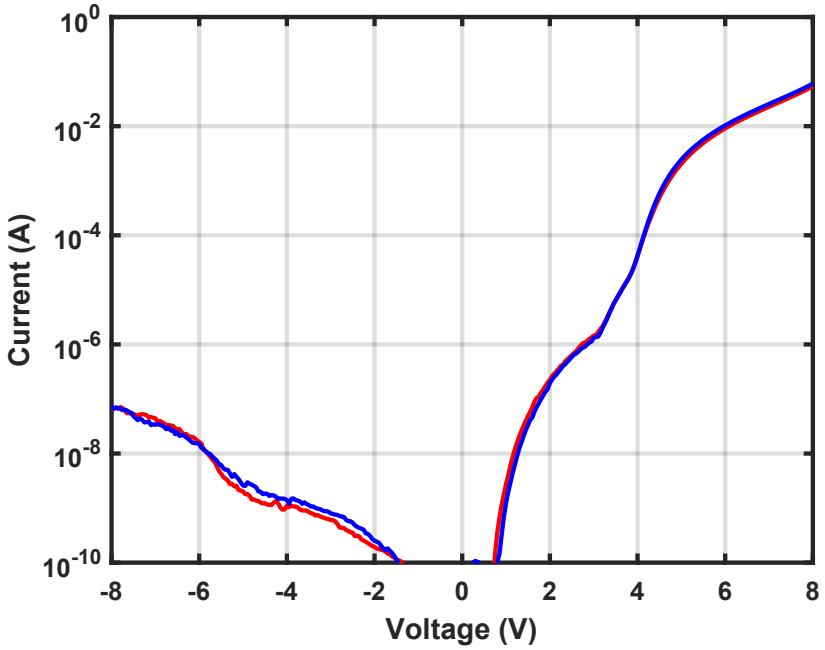

Figure 2-29. Current plotted as a function of voltage on a log-y scale. Red trace is data taken from +8 V -to- -8 V and blue trace is data taken from -8 V -to- +8 V.

Pulsed L-I-V measurements were used to extract both the current-voltage relation and the light-current relation. A pulsed current injection technique is used to avoid unwanted heating in the device. A new pulsed L-I-V test set was designed and constructed to achieve both the high operating voltage and current generally seen in AlGaN devices. A custom set of printed circuit boards (PCB)s were designed to interface between an Avtech high power current pulser (AV-107D-B) and a GGB probe card (MCW-29-3307-1) to allow for pulsed light-current-voltage (LIV) measurements. Shown in Figure 2-30 (a) is a simplified schematic of the connection between the current pulser and device under test (DUT). The Avtech current pulser uses a DB37 output cable with characteristic impedance of Z0 = 10.8 Ω. The DB37 cable is too cumbersome to directly attach to the probe card. Instead, a custom adaptor PCB was designed to breakout the DB37 cable into four smaller parallel SMPM cables. The four 50 Ω cables in parallel provided reasonably good impedance matching to the DB37 cable. Another custom interface PCB was then designed to directly (electrically and physically) attach to the probe card. The interface PCB accepts the four SMPM cables from the adaptor PCB and contains several resistor networks to impedance match and allow for measurement of the voltage and current at the DUT. A resistor network consisting of four parallel resistors (each with value RM) can be modified as needed to provide the desired input impedance matching. Optional Zener diodes (Z1×2) can be used for over-voltage protection at the DUT. The current through the DUT is measured using four parallel sense resistors (each with value RS). The voltage across the DUT is measured using a single shunt resistor (Rp). Multiple parallel components are used to reduce the parasitic inductance. SMPM cables are used to connect the output of the resistor networks to a 50 Ω terminated oscilloscope.

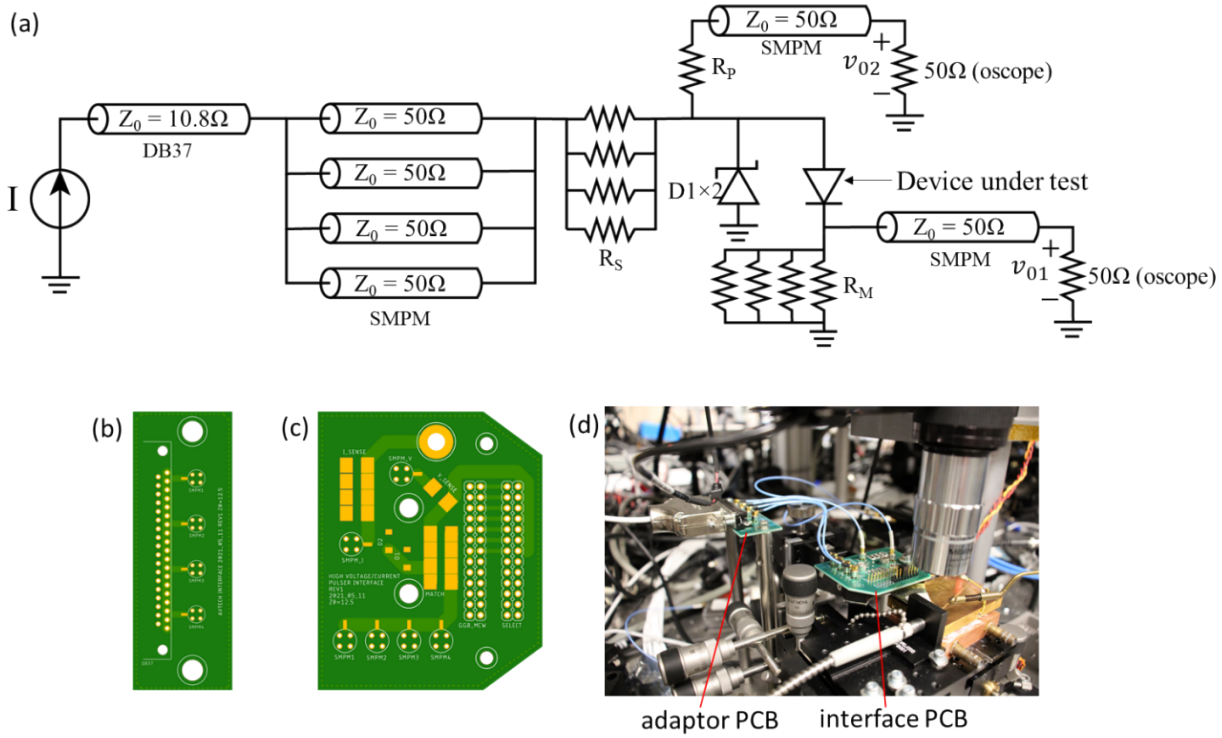

Figure 2-30. (a) Simplified schematic of current pulser test set; (b) rendering of unpopulated adaptor PCB and (c) interface PCB; and (d) image of pulsed LIV test set.

A rendering of the unpopulated adaptor and interface PCBs are shown in Figure 2-30 (b,c). An image of the current pulse setup is shown in Figure 2-30 (d). In the implementation shown here, the test setup is used to collect the output light with a fiber optic cable for spectroscopic measurement. The fiber optic assembly slightly obscures the probe card attached to the interface PCB in the image. Jumpers can be used on the header on the interface PCB to connect or disconnect individual probe tips to the current pulser output. This is useful if measuring short devices to avoid accidentally shorting out a probe tip on the stage.

The current through the DUT (I_DUT) can be related to the voltage at the 50 Ω terminated oscilloscope (v_o1) as

$$I_{DUT} = v_{o1}\frac{R_s + 200}{200R_s}$$

and the voltage across the DUT (V_{DUT}) can be related to the voltage at the oscilloscope (v_{o2}) as

$$V_{DUT} = v_{o2}\left(1 + R_p/50\right) - v_{01}.$$

Shown in Table 2-2 are the part numbers for the components that are currently used in the current pulse test setup.

Table 2-2. Component description and part numbers for the custom current pulser PCBs

Description	Schematic component	Manufacturer and part number(s)
Current pulser	I	Avtech AV-107D-B
DB37 cable Z_0 = 10.8 Ω	DB37	Avtech AV-CLZ11
DB37 connector	Not shown	TE Connectivity A23316-ND
SMPM cable	SMPM	Amphenol 7032-7525-ND Amphenol 7032-6354-ND
SMPM connector	Not shown	Amphenol SF3211-60034-ND
Zener diode	D1	Not currently implemented. Accepts STMicro 497-STPS2150AFNCT-ND
Impedance matching resistor	R_M	Currently shorted in existing implementation. Accepts Stackpole RHC2512 footprint.
Current sense resistor	R_S	Stackpole RHC2512FT1R00CT-ND 1Ω resistor (four of these resistors are in parallel for total resistance of 0.25Ω)
Voltage shunt resistor	R_P	Stackpole RHC2512FT1K00CT-ND 1kΩ resistor (two of these resistors are in parallel for total resistance of 500Ω)
Probecard	Not shown	GGB MCW-29-3307-1

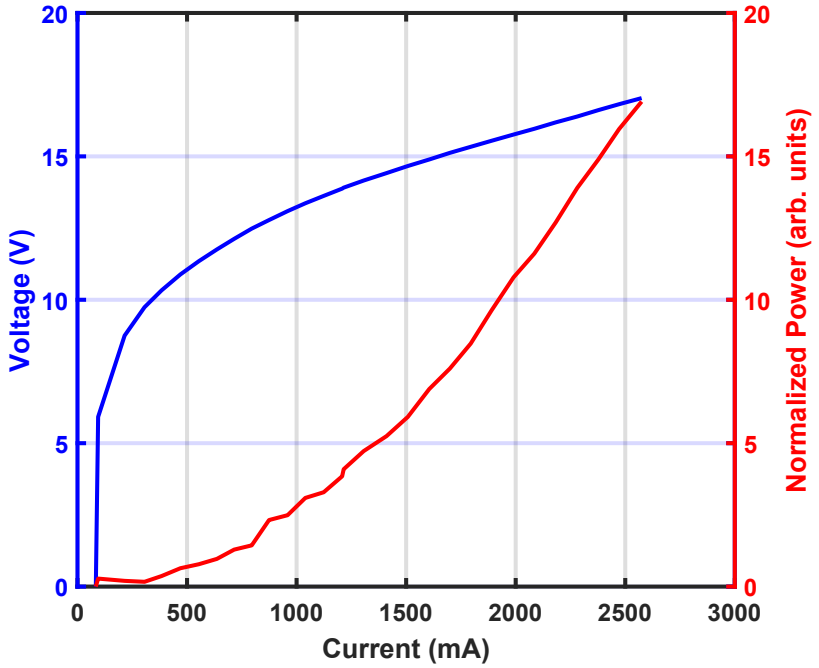

Figure 2-31. Pulsed LIV of diode bar showing super linear light output as a function of voltage, no threshold is reached.

The pulsed L-I-V for various devices lengths and ridge widths were captured using the new test set. A typical pulsed L-I-V is shown in Figure 2-31 showing a super-linear response in the light vs. current trace; but did not reach a laser threshold. Future efforts could use high-reflective coatings to try to improve the laser cavity quality factor and reach threshold. Another option would be to increase the optical gain by increasing the modal confinement factor by changing the position or number of quantum wells. We may also be losing current through lateral current leakage where current is able to leak around the region of high gain. This leakage problem was investigated using near-field imaging as described below.

Near-field images of the spontaneous emission from a single quantum well laser diode structure was measured by focusing the light onto a thermo-electric (TE)-cooled silicon CCD camera with an aspherical lens. Shown in Figure 2-32 (a) is an image of a laser structure with a 3.5 μm wide (as-drawn) waveguide. The laser structure was forward biased with 30 mA direct current. We observe bright light emission from an area that is consistent in size with the waveguide. The intensity line scan across the waveguide is plotted in Figure 2-32 (b) which shows that there is also light emission occurring outside of the waveguide region. The origin of this light emission is not fully understood but could be an imaging artifact related to imperfect focusing of the divergent light, scattered light that is reaching the camera, or light emission related to leakage current.

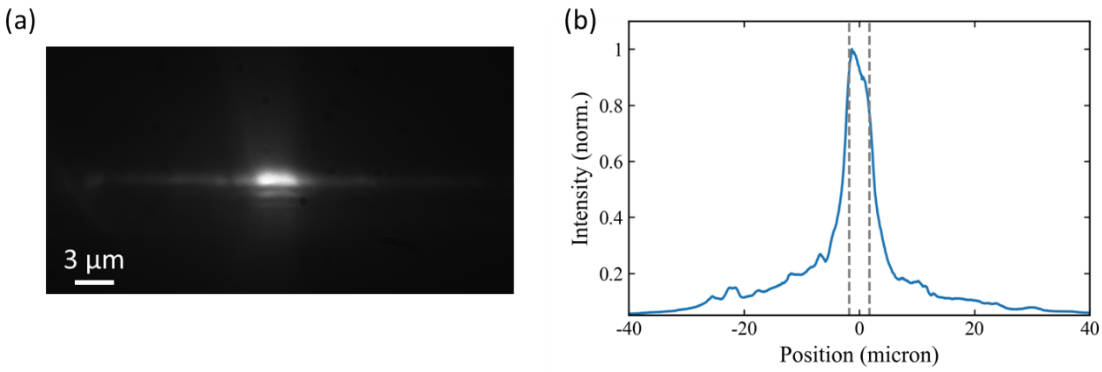

Figure 2-32. (a) Near-field image of the spontaneous emission emitted from the facet of the single quantum well laser structure; (b) intensity line scan from left-to-right in the image shown in (a). The dashed grey lines specify the location of the waveguide.

Finally, in Figure 2-33, we show sub-lasing-threshold EL of a representative laser as a function of pulsed current. Data were taken on a 1-mm-long device of ridge with ~ 11 μm and up to 400 mA, representing a current density of ~ 3.6 kA/cm^2. Up to this current density, which is much lower than that shown in Figure 2-31, the integrated EL intensity is approximately linear. The peak of the EL undergoes a minor blue shift, from 358.8 nm to 357.7 nm, from 60-400 mA injection current, revealing that the pulsed current testing has effectively mitigated the red shift that is typical of device heating. A line narrowing of ~ 1.3 nm is observed over the measured current range.

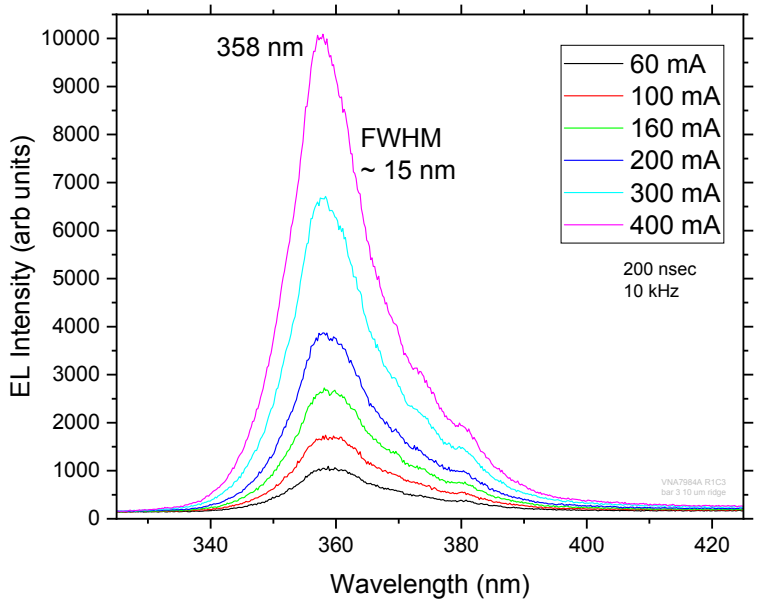

Figure 2-33. Electroluminescence spectra as a function of pulsed injection current.

3. SUMMARY

Throughout this project we were able to make some important advancements, and although we were not able to achieve a device that reached laser threshold, we have established capability that has already made an impact on other projects and will be leveraged for future projects.

The modeling effort was able to achieve advancements on two important thrusts: optical modeling and electrical modeling. In the optical modeling thrust we established a capability to account for the directional birefringence for hexagonal lattice III-N materials. In addition, we also established the capability to implement compositional gradients in the optical mode solver which was useful once it was clear that polarization doping was found to be successful in both modeling and experimentally. The electrical modeling was able to predict the experimental results from polarization doping publications. Later, the electrical modeling was used to inform the laser designs that included polarization doping compositional gradients. Important insight was gained in the proximity of the p-type doping to the MQW and experimental electroluminescence results validated the model.

Electroluminescence was used to quickly test different material stacks for relative efficiency in light emission. Added capability to the test set which allowed automated bias current sweeps allowed us to gain insight to the evolution of the light output efficiency and the relation to the deep state emission. Using this knowledge allowed us to be selective in the device designs that were selected for full ridge waveguide laser structure fabrication.

Advancements in the epitaxial growth were shown to reduce the cracking of the epilayers which is important for the ridge waveguide laser structure designs. This advancement was due to optimization of growth conditions and the use of a new 2D substrate pattern which provides some strain relaxation and a reduction in the epilayer cracking. We were also able to show polarization doping through various experimental means and that a reduction in the concentration of Mg in the structure still results in activated hole carriers. This important proof of principle can be used for various III-N structures moving forward.

Fabrication of laser structures was improved throughout the project; we found that the main difficulties of processing ridge waveguide structures were epitaxial defects and the shallow ridge waveguide etch depth, which hindered self-aligned ridge waveguide pad metal formation. Wafer bowing was also found to make the achievement of uniform ridge waveguide width across the wafer extremely difficult. We implemented a new process to expose the metalized ridge waveguide top more easily but found that the epitaxial defects were not sufficiently isolated from the pad metal and shunt diodes could be formed between the metal and the n-type material. A further process change used a BCB polymer to overcome this issue and we believe that this will be beneficial for future projects.

Finally, we were able to find diodes with minimal shunt diodes such that we could obtain I-V sweeps. The I-V sweeps showed several inflection points that indicate that indeed there are parasitic shunt diodes that have a lower turn-on voltage than the main diode. This will steal current from the device and, we found, eventually cause a catastrophic shunt resistance. The modified BCB process should avoid this type of failure mode. Advanced defect isolation process techniques based on surface-scanning and laser writing could also be used to advance the state of art of defect isolation process techniques. Pulsed L-I-V sweeps were taken to extract the light vs. current of various ridge waveguide structures where we found super-linear behavior, but no threshold was reached. We believe that either an increase of the cavity quality factor or an increase in the modal gain would be beneficial.

4. REFERENCES

[1] H. Yoshida, Y. Yamashita, M. Kuwabara and H. Kan, "Demonstration of an ultraviolet 336 nm AlGaN multiple-quantum-well laser diode," *Applied Physics Letters,* vol. 93, no. 24, p. 241106, 2008.

[2] Z. Zhang, M. Kushimoto, T. Sakai, N. Sugiyama, L. J. Schowalter, C. Sasaoka and H. Amano, "A 271.8 nm deep-ultraviolet laser diode for room temperature operation," *Applied Physics Express,* vol. 12, no. 12, p. 124003, 2019.

[3] J. Simon, V. Protasenko, C. Lian, H. Xing and D. Jena, "Polarization-Induced Hole Doping in Wide–Band-Gap Uniaxial Semiconductor Heterostructures," *Science,* vol. 327, no. 5961, pp. 60-64, 2010.

[4] H. Taketomi, Y. Aoki, Y. Takagi, A. Sugiyama, M. Kuwabara and H. Yoshida, "Over 1 W record-peak-power operation of a 338 nm AlGaN multiple-quantum-well laser diode on a GaN substrate," *Japanese Journal of Applied Physics,* vol. 55, no. 5, 2016.

[5] K. Nagata, K. Takeda, K. Nonaka, T. Ichikawa, M. Iwaya, T. Takeuchi, S. Kamiyama, I. Akasaki, H. Amano, H. Yoshida, M. Kuwabara, Y. Yamashita and H. Kan, "Reduction in threshold current density of 355 nm UV laser diodes," *Physica Status Solidi (c),* vol. 8, no. 5, pp. 1564-1568, 2011.

[6] H. Yoshida, M. Kuwabara, Y. Yamashita, Y. Takagi, K. Uchiyama and H. Kan, "AlGaN-based laser diodes for the short-wavelength ultraviolet region," *New Journal of Physics,* vol. 11, no. 12, p. 125013, 2009.

[7] K. Iida, T. Kawashima, A. Miyazaki, H. Kasugai, S. Mishima, A. Honshio, Y. Miyake, M. Iwaya, S. Kamiyama, H. Amano and I. Akasaki, "350.9 nm UV Laser Diode Grown on Low-Dislocation-Density AlGaN," *Japanese Journal of Applied Physics,* vol. 43, no. 4, p. 499, 2004.

[8] A. Allerman, M. Crawford, S. Lee and B. Clark, "Low dislocation density AlGaN epilayers by epitaxial overgrowth of patterned templates," *Journal of Crystal Growth,* vol. 388, pp. 76-82, 2014.

[9] S. R. Lee, A. M. West, A. A. Allerman, K. E. Waldrip, D. M. Follstaedt, P. P. Provencio, D. D. Koleske and C. R. Abernathy, "Effect of threading dislocations on the Bragg peakwidths of GaN, AlGaN, and AlN heterolayers," *Applied Physics Letters,* vol. 86, no. 24, p. 241904, 2005.

[10] A. Armstrong, A. A. Allerman, T. A. Henry and M. H. Crawford, "Influence of growth temperature on AlGaN multiquantum well point defect incorporation and photoluminescence efficiency," *Applied Physics Letters,* vol. 98, no. 16, p. 162110, 2011.

[11] A. Armstrong, M. W. Moseley, A. A. Allerman, M. H. Crawford and J. Wierer, "Growth temperature dependence of Si doping efficiency and compensating deep level defect incorporation in Al0.7Ga0.3N," *Journal of Applied Physics,* vol. 117, no. 18, p. 185704, 2015.

[12] M. H. Crawford, A. A. Allerman, A. M. Armstrong, M. L. Smith and K. C. Cross, "Laser diodes with 353 nm wavelength enabled by reduced-dislocation-density AlGaN templates," *Applied Physics Express,* vol. 8, no. 11, p. 112702, 2015.

[13] Z. L. Liau, R. L. Aggarwal, P. A. Maki, R. J. Molnar, J. N. Walpole, R. C. Williamson and I. Melngailis, "Light scattering in high-dislocation-density GaN," *Applied Physics Letters,* vol. 69, no. 12, pp. 1665-1667, 1996.

[14] S. Tanaka, Y. Kawase, S. Teramura, S. Iwayama, K. Sato, S. Yasue, T. Omori, M. Iwaya, T. Takeuchi, S. Kamiyama, I. Akasaki and H. Miyake, "Effect of dislocation density on optical gain and internal loss of AlGaN-based ultraviolet-B band lasers," *Applied Physics Express,* vol. 13, no. 4, p. 45504, 2020.

[15] J. Klootwijk and C. Timmering, "Merits and limitations of circular TLM structures for contact resistance determination for novel III-V HBTs," in *Proceedings of the 2004 International Conference on Microelectronic Test Structures (IEEE Cat. No.04CH37516)*, 2004.

[16] D. Z. Garbuzov, M. A. Maiorov, V. Khalfin, M. G. Harvey, A. Al-Muhanna, L. J. Mawst, D. Botez and J. C. Connolly, "Super-high-power operation of 0.98-μm InGaAs(P)/InGaP/GaAs-broadened waveguide separate confinement heterostructure quantum well diode lasers," in *Physics and simulation of optoelectronic devices. Conference*, 1999.

[17] T. Fan, "Laser beam combining for high-power, high-radiance sources," *IEEE Journal of Selected Topics in Quantum Electronics,* vol. 11, no. 3, pp. 567-577, 2005.

[18] S. Zhao, X. Liu, S. Y. Woo, J. Kang, G. A. Botton and Z. Mi, "An electrically injected AlGaN nanowire laser operating in the ultraviolet-C band," *Applied Physics Letters,* vol. 107, no. 4, p. 43101, 2015.

[19] L. J. Mawst, A. Bhattacharya, J. Lopez, D. Botez, D. Z. Garbuzov, L. DeMarco, J. C. Connolly, M. Jansen, F. Fang and R. F. Nabiev, "8 W continuous wave front-facet power from broad-waveguide Al-free 980 nm diode lasers," *Applied Physics Letters,* vol. 69, no. 11, pp. 1532-1534, 1996.

DISTRIBUTION

Email—Internal

Name	Org.	Sandia Email Address
Mary Crawford	1800	mhcrawf@sandia.gov
Michael Smith	1873	mlsmith@sandia.gov
Andrew Allerman	1876	aaaller@sandia.gov
Charles Alford	5264	cralfor@sandia.gov
Kenneth Dean	5264	kadean@sandia.gov
Seth Fortuna	5264	sfortun@sandia.gov
Erik Skogen	5264	ejskoge@sandia.gov
Technical Library	01977	sanddocs@sandia.gov

Sandia National Laboratories

Sandia National Laboratories is a multimission laboratory managed and operated by National Technology & Engineering Solutions of Sandia LLC, a wholly owned subsidiary of Honeywell International Inc. for the U.S. Department of Energy's National Nuclear Security Administration under contract DE-NA0003525.